Influence of Head Tissue Conductivity Anisotropy on Human EEG and MEG using Fast High Resolution Finite Element Modeling, based on a Parallel Algebraic Multigrid Solver

Carsten H. Wolters[1,2]
Alfred Anwander[2]
Martin A. Koch[2,3]
Stefan Reitzinger[4]
Michael Kuhn[4,5]
Markus Svensén[2]
[1] Max Planck Institute for Mathematics in the Sciences, Leipzig
[2] Max Planck Institute of Cognitive Neuroscience, Leipzig
[3] Universitätsklinikum Hamburg-Eppendorf, Neurologische Klinik, Hamburg
[4] Institute for Comp. Math., J. Kepler Univ., Linz, Austria
[5] Bruker Saxonia Analytik GmbH, Leipzig

Abstract

Accuracy and time play an important role in medical and neuropsychological diagnosis and research. The inverse problem in the field of Electro- and MagnetoEncephaloGraphy requires the repeated simulation of the field distribution for a given dipolar source in the human brain using a volume-conduction model of the head. High resolution finite element head modeling allows the inclusion of tissue conductivity inhomogeneities and anisotropies. We will present new approaches for individually determining the direction-dependent conductivities of skull and brain white matter, based on non-invasive multimodal magnetic resonance imaging data, and for generating a high resolution realistic anisotropic finite element model of the human head. Error estimations will indicate the necessity of the chosen complex forward model. The finite element approach within the inverse problem leads to a sparse, large scale, linear equation system with many different right hand sides to be solved. The presented solution process is based on a parallel algebraic multigrid method. It is shown that very short computation times can be achieved through the combination of the multigrid technique and the parallelization on distributed memory computers. The iterative solver approach is shown to be stable towards modeling of tissue anisotropy. A solver time comparison to a classical parallel Jacobi preconditioned conjugate gradient method is given.

Acknowledgements

This work has been supported by Prof. E. Zeidler, director of the MPI for Mathematics in the Sciences Leipzig, by the Leibniz-Prize of the German Research Foundation awarded to Prof. A. D. Friederici, director of the MPI of Cognitive Neuroscience Leipzig, by the IST-program of the European Commission, project No.10378, SimBio (http://www.simbio.de), and by the Austrian Science Fund – ’Fonds zur Förderung der wissenschaftlichen Forschung’ – within the SFB F013 ”Numerical and Symbolic Scientific Computing”. We are particularly thankful to the following colleagues: S.Burkhardt (Munich University of Technology), F. Kruggel, G. Lohmann and B.Maess (MPI of Cognitive Neuroscience Leipzig).

1 Introduction

Nowadays devices and tools are available for analyzing and monitoring the human brain at a high level of detail. These details are necessary, e.g., for successful surgery or, more generally, for basic brain research. Often computational methods are used in the diagnostic and pre-surgical phase. Such non-invasive tools are of course preferable to invasive methods, e.g., surgery, with high risks for patients. In fundamental brain research, most often there is no other choice besides computational methods. However, the acceptance of tools depends very much on their reliability and robustness and on their speed. In this article it will be shown how non-invasive imaging methods deliver necessary data for such a tool and how advanced numerical methods enhance its accuracy and speed. The article brings together clinical diagnosis, pre-surgical planning, clinical and cognitive research and numerical mathematics, and describes the needed imaging data and the requirements of necessary algorithms and software.

It is common practice in cognitive research and in clinical routine and research to localize current sources in the human brain by means of the induced electric potentials, measured with electrodes which are fixed on the scalp (ElectroEncephaloGraphy, EEG) and/or the induced magnetic flux density, measured in a distance of a few centimeters from the head surface (Magne-

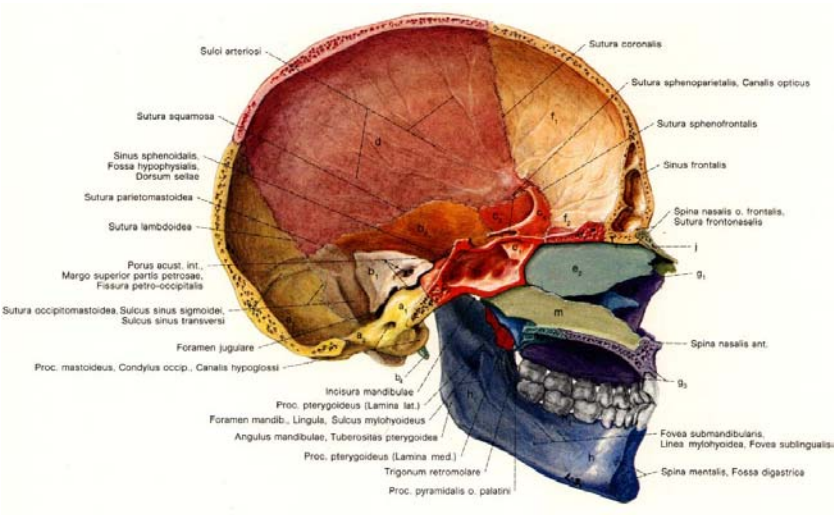

Fig. 1: The human skull: Suture lines and the tri-layeredness [Platzer,1994].

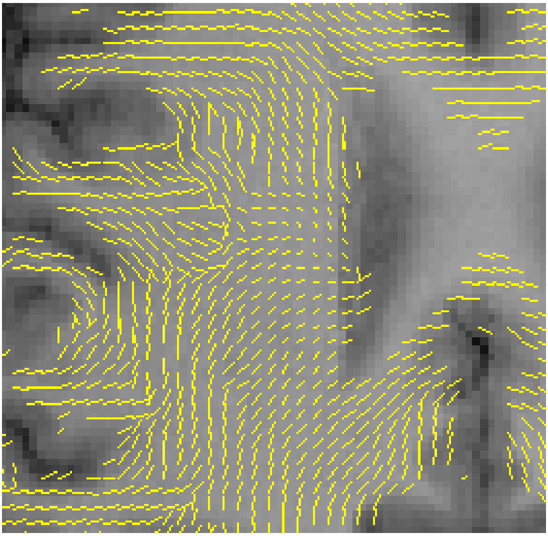

Fig. 2: Fibre orientation map from a DT-MRI experiment [Wolters et al.,1999b]. Eigenvector orientations corresponding to the largest eigenvalue are projected onto the imaging plane, and overlaid on a T1 weighted MRI. Eigenvector directions were suppressed in voxels with $FA <$ 0.2 (see Definition for FA in Equation (11))

toEncephaloGraphy, MEG). The localization of the underlying source distribution is an inverse problem whose solution requires the repeated simulation of the electric/magnetic fields in the head for a varying source in the brain (forward problem). For the forward problem, the volume-conductor head has to be modeled. An overview of the head tissues with different conductivities can be found in [Haueisen, 1996]. The human skull consists of a soft bone layer (spongiosa) enclosed by two hard bone layers (compacta). Since the spongiosa have a much higher conductivity than the compacta [Akhtari *et al.*, 2000], the skull shows a direction-dependent (anisotropic) conductivity with an anisotropy ratio of up to 1:10 (radially:tangentially to the skull surface) [Akhtari *et al.*, 2000]. Skull anisotropy was shown to have an impact on the inverse problem in EEG [Marin, 1997; Marin *et al.*, 1998]. Figure 1, taken from [Platzer, 1994], illustrates geometrical features of the human skull.

It is known that brain white matter has an anisotropic conductivity with a ratio of about 1:9 (normal:parallel to fibers) [Nicholson, 1965], but still, no technique exists for a robust and non-invasive direct measurement of conductivity anisotropy in the whole brain. Recently, formalisms have been described for relating the effective electrical conductivity tensor of white matter tissue to the effective water diffusion tensor as measured by Diffusion Tensor Magnetic Resonance Imaging (DT-MRI). Fig. 2 shows a white matter fibre orientation map from a DT-MRI experiment [Wolters *et al.*, 1999b]. [Basser *et al.*, 1994b] introduced the assumption that the effective electrical conductivity tensor shares the eigenvectors with the effective diffusion tensor of water, which can be measured for white matter tissue by DT-MRI. [Tuch *et al.*, 1998; Tuch *et al.*, 1999] proposed a linear relationship between the eigenvalues of both tensors for small intracellular diffusion and high resistivity of the cell membrane. Their proposition is based on a self-consistent differential Effective Medium Approach (EMA) for the generalized dielectric constant (for low frequencies the conductivity) of porous media, derived from a multiple scattering formula from solid state physics developed by [Sen *et al.*, 1981]. [Latour *et al.*, 1994] derived a similar EMA for the effective water diffusion in biological cells. The coupling of both EMA-formulae through the unknown porosity variable led to the linear dependence of the eigenvalues described in [Tuch *et al.*, 1998]. In a first study, white matter conductivity anisotropy was shown to have an influence on EEG and MEG [Haueisen *et al.*, 2002].

In this article, we will present measurement techniques and methods for obtaining a realistically shaped high resolution volume conductor model of the human head in a non-invasive way with anisotropically conducting compartments skull and white matter. Our goal is the study of the influence of tissue anisotropy on EEG and MEG.

A bottleneck for such sensitivity studies towards the different inverse source reconstruction techniques and especially for broad application of high resolution volume conductor modeling to inverse reconstructions in the application fields is the time for calculating the 3D potential distributions during the various forward problems that have to be solved. [Waberski *et al.*, 1998], e.g., conclude that for the achievement of the final goal in epilepsy source localization, i.e., the general clinical use, realistically shaped high resolution head models are necessary and parallel computing has to speed up the computation. Finite Element (FE) models for the electromagnetic field simulation in the head have been developed by various research groups (see e.g. [Bertrand *et al.*, 1991; Haueisen, 1996; van den Broek *et al.*, 1997; Buchner *et al.*, 1997; Awada *et al.*, 1997; Marin *et al.*, 1998]). The FE method is able to treat geometries of arbitrary shape and inhomogeneous and anisotropic material parameters. Generally iterative solvers like the preconditioned Conjugate Gradient (CG) method with conventional preconditioners on single processor machines have been used for the large linear equation system arising from this approach. The hundred or even thousand times repeated solution of such a system with a constant stiffness matrix and varying right hand sides is the major time consuming part within the inverse localization process. These calculation times limited the resolution of the models or, even worse, the broader application of anisotropic FE based head modeling to practical source localization problems got stuck.

Geometric MultiGrid (GMG) methods have proven to be of optimal order with respect to arithmetic costs and memory requirement, see e.g. [Hackbusch, 1985]. In [Jung and Langer, 1991], it was shown that multigrid methods are efficient preconditioners for the conjugate gradient method. For a parallel implementation see for instance [Bastian *et al.*, 1997]. GMG methods suffer from the requirement of a grid hierarchy, which is not available in our case. By contrast, Algebraic MultiGrid (AMG) methods use only single grid information (see e.g. [Ruge and Stüben, 1986; Braess, 1995; Kickinger, 1998; Haase *et al.*, 2000; Reitzinger, 2001] and for parallel versions [Falgout *et al.*, 1999; Krechel and Stüben, 2001; Haase *et al.*, 2002; Wagner, 2000]) while mostly preserving the properties of the geometric version. Many numerical studies have shown a good performance of AMG preconditioners. Furthermore, AMG preconditioners were successfully applied to source localization recently ([Wolters *et al.*, 2000; Johnson *et al.*, 2000]). Even if AMG preconditioned CG (AMG-CG) was shown to be very fast in comparison to standard methods, additional speedup is required. In [Wolters *et al.*, 2002], we described for realistically shaped isotropic high resolution tetrahedra and cube head models how the latter can be achieved by using a parallel computer with a moderate number of processors. Within this article, we will show that our approach is stable towards realistic head tissue anisotropy.

Subsection 1.1 of this article will give an overview of different application fields of source localization and will present an exemplary reconstruction result for Somatosensory Evoked Potentials (SEP). It aims at giving further motivation for readers from outside the bioelectromagnetism area and it can be skipped otherwise. In Section 2, the modeling aspects for the forward problem will be described. Subsection 2.1 gives an overview of a physical model for the source and for the field distribution in the head volume conductor. In 2.2, we will describe the generation process of a realistically shaped anisotropic 5-tissue head model. We focus on the modeling aspect for obtaining an anisotropically conducting skull in 2.2.1 and an anisotropically conducting white matter compartment in 2.2.2, using multimodal Magnetic Resonance Imaging (MRI) data. The section terminates with FE meshing and discretization aspects for EEG and MEG in 2.3. In Section 3, the AMG-CG solver is described as a fast solver for the large linear equation system arising from the FE approach. The partitioning of the meshes and a parallelization strategy for distributed memory computers will then be presented. Section 4 describes the new software developments. In the first part of Section 5, we will present results concerning the influence of tissue conductivity anisotropy on EEG and MEG for various simulated sources. Performance results of the parallel AMG solver and its sensitivity to tissue anisotropy will be discussed in the second part. The parallelized multigrid method will be compared with a parallel Jacobi-preconditioned CG method (Jacobi-CG), which is a well-known solver method in FE source localization. It will be shown that high speedups can be achieved which open the possibility for a broader application of high resolution realistically shaped anisotropic FE based source localization in the human brain. The article ends with the conclusions in Section 6.

1.1 Overview of applications of source localization

This subsection is only meant to be a further motivation and to list some references for readers who would like to know more about the inverse problem and some well-established application fields of EEG/MEG-source localization.

An overview of the different application fields of source localization can be found in [Andrä and Nowak, 1998]. Various inverse reconstruction techniques for continuous and discrete source parameter spaces are described, e.g., in [Scherg and von Cramon, 1985; Buchner *et al.*, 1997; Knösche, 1997; Wagner, 1998; Wolters *et al.*, 1999a; Schmitt and Louis, 2002; Schmitt *et al.*, 2002].

A first example is the study of functional cortical organization by means of evoked fields of the somatosensory system. The different evoked signal components of interest in such studies appear during the first 100 ms post-

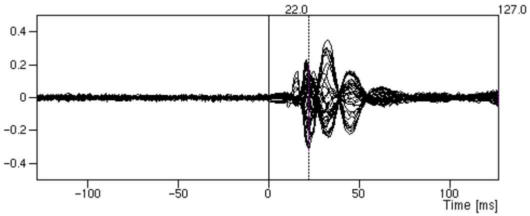

Fig. 3: SEP example dataset, taken from CURRY: Butterfly plot of averaged EEG data from -0.4 *to* $0.4\ \mu V$*. The P22 signal component is marked.*

stimulus. Since the components are well time-locked and not dependent on the attention of the subjects, the signal can be averaged over a large number of trials so that the signal components of interest are obtained with a relatively good signal-to-noise ratio. Figure 3 shows the averaged EEG measurements for SEP in 31 channel butterfly plot from [Fuchs *et al.*, 1998], included as an example dataset in the software package [CURRY, 2000]. As an example for a medically interesting source localization result, the continuous dipole fit method, introduced by [Scherg and von Cramon, 1985], with two dipoles at the peak of the SEP-P22 signal component is shown in Figure 4 (see [Fuchs *et al.*, 1998]). The result has been calculated using the example dataset and methods within [CURRY, 2000]. Source localization methods have also been

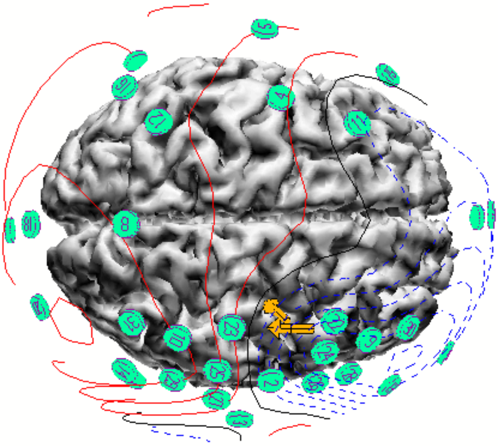

Fig. 4: SEP source localization example, computed with CURRY: Results of the continuous dipole fit method with two dipoles at the peak of the P22 signal component.

introduced to characterize the generators of signals related to higher cognitive function. An example is a recent study showing equivalences between speech and music processing in the brain [Maess *et al.*, 2001].

The non-invasive EEG/MEG-source localization diagnosis method is successfully used in clinical research and application. For instance tumors may distort brain anatomy so that the presurgical localization of sensory or motor areas on the basis of anatomical landmarks is impossible. In [Sutherling *et al.*, 1988], the agreement between invasive and non-invasive methods was evaluated and an "excellent precision of the source localization results" was found. About 0.25 % of the world population suffers from drug-resistant epilepsy and about 10 to 15 % would profit from a surgical removement of the epileptogenic tissue [Andrä and Nowak, 1998]. As opposed to alternative invasive diagnostic procedures, i.e., opening the skull and implanting electrodes near the assumed focus (ECoG surface electrodes or depth electrodes) which put the patient under a considerable risk and is cost intensive, source localization procedures are non-invasive and can give a more "global" overview since the sensors can be placed around the whole head. [Waberski *et al.*, 1998], e.g., found a high congruence of source reconstruction and invasive determination of the focus of epileptiform activity using realistically shaped head models.

2 The forward problem

2.1 *Physical modeling*

The sources to be localized during the inverse problem and to be modeled in the forward problem are electrolytic currents within the dendrites of the large pyramidal cells of activated regions in the cortex sheet of the human brain. Stimulus-induced activation of a large number of excitatory synapses of a whole pattern of neurons leads to a negative monopole under the brain surface, whereas the cells in rest form a positive monopole quite closely underneath. The stimulus can have various forms, e.g., any visual or auditory stimulus in neuropsychological experiments or an epilepsy- or tumor-induced stimulus as clinical examples. The resulting primary current is generally formulated as a mathematical dipole

$$\vec{j}^p\,(\vec{x}) = \vec{M}\delta(\vec{x} - \vec{x}_0) \tag{1}$$

at the position $\vec{x}_0$ with the moment $\vec{M}$ (see e.g.[de Munck *et al.*, 1988]). The dipole source establishes an electric field $\vec{E}$ and a return current $\sigma\vec{E}$ in the whole head with σ denoting the 3×3 conductivity tensor. The total current distribution $\vec{j}$ in the head is then modeled as

$$\vec{j} = \vec{j}^p + \sigma\vec{E}.$$

Since in the considered low frequency band (frequencies below 1000 Hz) the capacitive component of tissue impedance and the electromagnetic propagation effect can be neglected [Plonsey and Heppner, 1967], the fields are quasistatic and $\vec{E}$ can be expressed as the negative gradient of a scalar potential Φ, so that

$$\vec{j} = \vec{j}^p - \sigma \nabla \Phi .$$

Because the divergence of $\vec{j}$ must be zero, we arrive at the quasistatic approach of Maxwell's equations of electrodynamics

$$\nabla \cdot (\sigma \nabla \Phi) = J^p = \nabla \cdot \vec{j}^p \tag{2}$$

in Ω with appropriate boundary conditions

$$\sigma \frac{\partial \Phi}{\partial \vec{n}} \bigg|_{\Gamma} = 0 \tag{3}$$

with Ω denoting the head, Γ the head surface and $\vec{n}$ the surface normal. Additionally, a reference electrode with given potential is assumed, i.e.,

$$\Phi_{ref} = 0\,. \tag{4}$$

For the magnetic problem, linear material equations are used and it is assumed, that the magnetic permeability, μ, is constant over the whole volume and equal to the permeability of vacuum, so that the following quasistatic Maxwell equation for the flux density $\vec{B}$ is valid [Sarvas, 1987]:

$$\nabla \times \vec{B} = \mu \vec{j}. \tag{5}$$

Since the divergence of $\vec{B}$ is zero, a magnetic potential $\vec{A}$ with $\vec{B} = \nabla \times \vec{A}$ can be introduced and, using Coulomb's gauge $\nabla \cdot \vec{A} = 0$, Equation (5) transforms to

$$\mu \left(\vec{j}^p - \sigma \nabla \Phi \right) = \nabla \times \left(\nabla \times \vec{A} \right) = \nabla \left(\nabla \cdot \vec{A} \right) - \Delta \vec{A} = -\Delta \vec{A}.$$

The source term is vanishing outside the volume conductor, so that the solution of Poisson's equation is [Nolting, 1992]

$$\vec{A}(\vec{x}) = \frac{\mu}{4\pi} \int\limits_{\Omega} \frac{\vec{j}^p(\vec{y}) - \sigma(\vec{y}) \nabla \Phi(\vec{y})}{|\vec{x} - \vec{y}|} d\vec{y}. \tag{6}$$

Finally, the magnetic flux Ψ through an MEG magnetometer flux transformer Υ (see, e.g., Figure 13, left) is determined as an integral over the coil area F enclosed by Υ, or, using Stokes theorem, as

$$\Psi = \int\limits_{F} \vec{B}(\vec{x}) d\vec{x} = \oint\limits_{\Upsilon} \vec{A}(\vec{x}) d\vec{x}.$$

With

$$\vec{C}(\vec{y}) = \oint\limits_{\Upsilon} \frac{1}{|\vec{x} - \vec{y}|} d\vec{x}, \tag{7}$$

the final equations for primary magnetic flux, Ψ_p, and secondary magnetic flux, Ψ_s, emerging from primary and secondary (return) currents, resp., are given by

$$\begin{aligned}
\Psi_p &\overset{(1)}{=} \frac{\mu}{4\pi} < \vec{M}, \vec{C}(\vec{x}_0) > && (8)\\
\Psi_s &= \frac{-\mu}{4\pi} \int\limits_{\Omega} < \sigma(\vec{y}) \nabla \Phi(\vec{y}), \vec{C}(\vec{y}) > d\vec{y} && (9)\\
\Psi &= \Psi_p + \Psi_s.
\end{aligned}$$

[de Munck and Peters, 1993] derived series expansion formulas for problem (2) with boundary conditions (3) and reference potential (4) in order to calculate the potential distribution for a dipolar source in a multi-layer spherical shell model with constant isotropic or anisotropic conductivity values/tensors within each layer. It is now widely known that realistically shaped models of the human head are necessary to keep the localization error at an acceptable level (see e.g. [Waberski *et al.*, 1998]).

2.2 Generation of a realistic 5 tissue anisotropic head model

A prerequisite for a realistic modeling of the volume conductor is the segmentation of head tissues with different conductivity properties. MRI is known as a safe and non-invasive method for imaging the human head and does not expose subjects to radiation load like in Computed Tomography. The identification of the CerebroSpinal Fluid(CSF)-skull boundary based on T1-MRI (T1-weighted MRI) is problematic, and PD-MRI (Proton-Density-weighted MRI) is most appropriate for this task. Figure 5 shows an axial slice of the segmented 5-tissue head model and the corresponding slices of T1- and PD-MRI. The model will be used throughout this article. For the segmentation of skin, white and gray matter surfaces, we only refer to [Wolters, 2002], whereas we will now focus on the description of the modeling for the two anisotropic compartments, skull and white matter.

2.2.1 Generation of an anisotropic skull layer

The exact modeling of the low-conducting anisotropic human skull is of particular importance for EEG source localization [Burkhardt *et al.*, 2002; Huiskamp *et al.*, 1999]. The skull can be seen as an isolating layer which

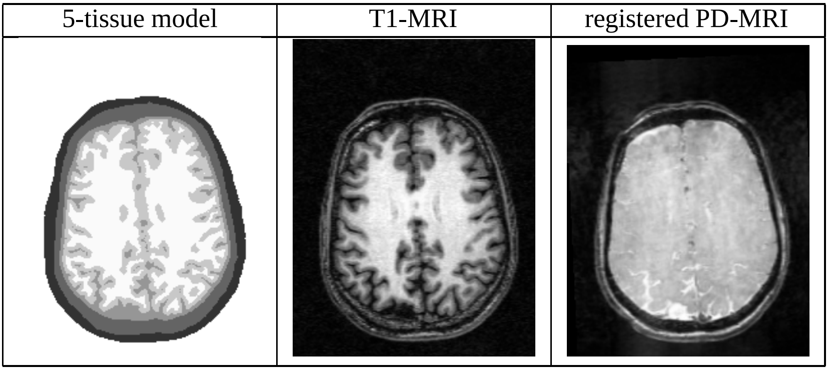

Fig. 5: Axial slice of the 5-tissue segmentation result and the corresponding slice of the T1-MRI and of the registered PD-MRI.

leads to a strong decrease and a blurring of the potential distribution towards the measurement electrodes.

A first step in the modeling process is the segmentation of inner and outer skull surfaces. We will now shortly summarize our results, see [Burkhardt *et al.*, 2002] for a deeper study. The registration of a bimodal data set is a fundamental step in order to exploit the information in both images in the segmentation process. Inspired by [Maes *et al.*, 1997], we used a voxel-similarity based registration method, yielding high accuracy in matching both modali-

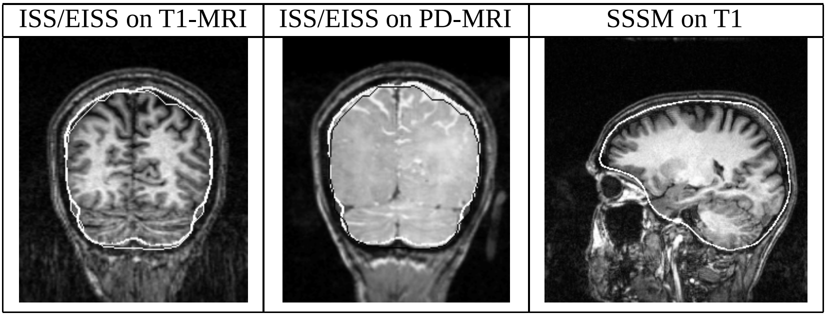

Fig. 6: Left and middle: Comparison of the segmented Inner Skull Surface (ISS) from bimodal MR images (bold white) and the Estimated Inner Skull Surface (EISS) by means of a T1-MRI based closing and inflation procedure (white on underlying T1 MRI and black on underlying registered PD MRI). Right: Smooth Surface Spongiosa Model (SSSM) on underlying T1-MRI for modeling the eigenvectors of the skull conductivity tensors.

ties [Burkhardt *et al.*, 2002]. Figures 5 and 6 show the PD-MRI, which was registered onto the T1 image. Our segmentation approach for inner and outer skull surfaces uses a combination of basic 3D image operations, a fuzzy segmentation method which compensates for image intensity inhomogeneities, an extended region growing concept and a deformable model, exploiting the registered bimodal data set [Burkhardt *et al.*, 2002]. The bimodal MRI approach was shown to substantially improve the Inner Skull Surface (ISS) segmentation when compared to a T1-MRI based method. The latter estimates the inner skull from a segmentation of the cortical surface. The cortex surface is closed and inflated by a fixed distance via mathematical morphology to provide the Estimated Inner Skull Surface (EISS). The segmentation improvement was found to be large in particular in regions of the skull base, but also in those neurocranial roof areas with larger deviation between chosen global inflation parameter and realistic local thickness of the cerebrospinal fluid compartment [Burkhardt *et al.*, 2002]. The comparison of ISS and EISS segmentation results is shown in Figure 6 (left and middle). Errors in EEG source localization of up to 1cm in mesial-temporal and basal-frontal regions, resulting from inaccurate skull segmentation, were found in [Huiskamp *et al.*, 1999]. Since these regions are of particular importance in epilepsy surgery, it was concluded that this imprecision may be detrimental in clinical applications.

As mentioned in the introduction, the human skull is an anisotropically conducting layer, if it is regarded as one unit. [Marin, 1997; Marin *et al.*, 1998] pointed out the importance of well-defined skull conductivity tensor eigenvectors and reported larger errors for the EEG potential in the case of erroneous tensor directions. We therefore based our determination of tensor eigenvectors on the resulting mesh of a discrete deformable surface model, whose pseudo-code is shown in Algorithm 1. This model was also used for a segmentation improvement of inner and outer skull surface [Burkhardt *et al.*, 2002]. The deformable model was applied here in order to generate a Smooth Surface Spongiosa Model (SSSM), i.e., a strongly smoothed triangular mesh, which was shrunken from the outer skull mask onto the outer spongiosa surface. Therefore, the binary mask of the outer skull surface was shrunken by 2 under the assumption of a 2 mm thick outer compacta layer [Akhtari *et al.*, 2000], resulting in the initial binary $mask$. In a first step, the operation $EXTRACT$ extracts a triangle mesh from $mask$, using the marching tetrahedra method [Payne and Toga, 1990]. Then, the wrapper algorithm [Gueziec and Hummel, 1994] is applied to achieve a reduction in the vertex count to N_v vertices, while retaining the shape of the surface, denoted by the operation $SIMPLIFY$. $N_v = 30,000$ was found to be a good choice, since $mask$ is only moderately curved. The operation outputs a mesh with mesh vertices $\vec{v}^0$, normal vectors $\vec{n}^0$ and triangle elements Δ, where the normal vector for

Algorithm 1 DEFORM : $(mask, N_v, T1, I_{lim}, \omega_{in}, \omega_{ex}, it) \rightarrow SSSM$

```
$(\vec{v}^0, \vec{n}^0, \Delta) = SIMPLIFY(EXTRACT(mask), N_v)$, $i = 0$, $\kappa = 1/3$
for $i = 1$ up to $i = iters$ do
    for each of the $N_v$ vertices $\vec{v}^i$ do
        $\vec{F}_{in}(\vec{v}^i) = 0$                                  /* calculate smoothing force */
        for EACH OF THE $N$ EDGE-CONNECTED NEIGHBORS $\vec{v}^i_j$ OF $\vec{v}^i$ do
            $\vec{F}_{in}(\vec{v}^i) = \vec{F}_{in}(\vec{v}^i) + \frac{1}{N}\left(\vec{v}^i_j - \vec{v}^i\right)$
        end for
        $F_{ex,1}(\vec{v}^i) = \langle -\nabla I_g^{T1}(\vec{v}^i), \vec{n}^i \rangle$               /* gradient force */
        $F_{ex,2}(\vec{v}^i) = \tanh\left(\kappa(I^{T1}(\vec{v}^i) - I_{lim})\right)$           /* capturing force */
        $\vec{v}^{i+1} = \vec{v}^i + \omega_{in}\vec{F}_{in}(\vec{v}^i) + \omega_{ex}\left(F_{ex,1}(\vec{v}^i)F_{ex,2}(\vec{v}^i) + F_{ex,2}(\vec{v}^i)\right)\vec{n}^i$
    end for
    $i = i + 1$
end for
$SSSM = (\vec{v}^i, \vec{n}^i, \Delta)$
```

each vertex was calculated as the arithmetic mean of the neighboring triangle normals. The internal force $\vec{F}_{in}(\vec{v}^i)$ for a vertex in the i^{th} iteration, $\vec{v}^i$, is chosen as a force, which pulls the vertex to the centroid of its N edge-connected neighbor vertices. In order to force the SSSM to remain inside the segmented skull layer, the intensity values of all voxels inside the inner skull surface and outside the outer skull surface were set to the highest grey value 255, resulting in the modified image $T1$. The magnitude of the external force, acting along the vertex normal $\vec{n}^{\,i}$, is divided into two parts. The first, $F_{ex,1}$, is attached to the local intensity value gradient of the Gauss smoothed modified image, ∇I_g^{T1}, while the second term, $F_{ex,2}$, captures the surface within a narrow range around an image intensity I_{lim}. We chose I_{lim} as the arithmetic mean of the intensities of skull compacta and spongiosa. The parameter $\kappa \in \mathbb{R}$ defines the capturing range, which is related to the amount of noise in the MR data. It was fixed to $\kappa = 1/3$, following [Burkhardt *et al.*, 2002]. We performed $it = 100$ iterations with a strong weighting of the smoothing force, $\omega_{in} = 0.07$ and a moderate weighting for the external force, $\omega_{in} = -0.002$. The resulting triangle mesh $SSSM$ was voxelized and shown in Figure 6 (right). For each point in the skull layer, we are now able to determine the radial skull direction by means of the normal vector $\vec{n}^{\,k}$ of the SSSM vertex $\vec{v}^k$ with minimal distance. The two tangential directions in the perpendicular plane to the radial direction can then be determined using vector product. Within the simulations in Section 5, we use conductivity tensors of the form $\sigma = \mathbf{S}\mathbf{\Lambda}\mathbf{S}^T$ with $\mathbf{S}$ the orthogonal eigenvector matrix, built of the two tangential and the radial direction vectors, and simulated eigenvalues

$\mathbf{\Lambda} = \mathrm{diag}(\lambda_{tang}, \lambda_{tang}, \lambda_{rad})$, as described in Table 1 in Subsection 5.1.1.

2.2.2 Generation of an anisotropic white matter compartment

We performed whole-head-DTI using a 4-slice displaced U-FLARE [Norris and Börnert, 1993] protocol with centric phase-encoding. Diffusion weighting was implemented as a Stejskal-Tanner type spin-echo preparation [Koch, 2000]. Although echo planar imaging (EPI) is being widely applied for DTI purposes, U-FLARE was preferred to EPI in order to avoid spatial misregistration between the DTI data and the 3D data sets due to magnetic field inhomogeneities. The effective echo time was $T_{eff} = 120$ ms, and $TR = 11$ s. The diffusion weighting gradient pulses had a duration of 22 ms, and their onset was separated by 40 ms. Four different b values evenly spaced between 50 and 800 s/mm^2 were applied through variation of the gradient strength [Koch, 2000]. The slices were axially oriented and $5mm$ thick. In-plane resolution was 2×2 mm^2. In order to increase the signal-to-noise ratio, 5 to 16 images (depending on the b value) with identical diffusion weighting were averaged. Due to the long measurement time (50 min for 4 slices) data acquisition was split into 8 sessions. Diffusion tensor calculation [Basser *et al.*, 1994a] was based on a multivariate regression algorithm in IDL (Interactive Data Language, Research Scientific, Bolder, Colorado/USA). Figure 2 shows a detail of an axial slice of the measured DTI data with 2×2 mm^2 resolution on an underlying coregistered T1-MRI. The coregistered T1 images of the same slices allowed the registration of the DTI data on the 3D T1 data set. The registered DT data were then resampled to $1 \times 1 \times 1$ mm^3. In order to handle the orientation information in the registered DT images appropriately, each diffusion tensor $\mathbf{D}'$ was rotated with the rotation matrix $\mathbf{R}$ of the respective registration process via the similarity transform $\mathbf{D} = \mathbf{R}\mathbf{D}'\mathbf{R}^T$ [Alexander *et al.*, 2001]. Figure 7 shows $Tr(\mathbf{D})$, i.e., the sum of the diagonal tensor ele-

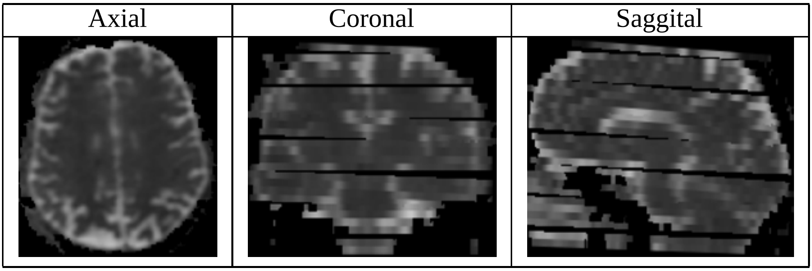

Fig. 7: $Tr(\mathbf{D})$ of the 8 registered DT-MRI sessions. Water diffusion coefficients in CSF (white) are much larger than in the brain, allowing a quality check of the registration.

ments, of the 8 registered DTI sessions. Since water diffusion coefficients in CSF are much larger than in the brain, a large contrast is achieved at the brain surface, which allows a quality check of the registration. As the figure shows, the registered DTI slices are not exactly parallel. Later in Subsection 2.3.1 for the generation of the FE volume conductor model, the gaps were filled with isotropic white matter conductivity tensors.

When extracting the anisotropic part of the diffusion tensor by means of

$$\mathbf{A} = \mathbf{D} - \frac{Tr\mathbf{D}}{3}\mathbf{I}, \tag{10}$$

we can define the "fractional anisotropy index" [Basser and Pierpaoli, 1996] as

$$FA = \sqrt{\frac{3}{2}}\frac{\sqrt{\mathbf{A}:\mathbf{A}}}{\sqrt{\mathbf{D}:\mathbf{D}}} \qquad \text{with} \quad \mathbf{B}:\mathbf{C} \equiv \sum_{i,j} B_{ij}C_{ij}. \tag{11}$$

Figure 8 shows a map of the fractional anisotropy index of the registered DT data, masked with the white matter mask of the 5-tissue segmentation result. The highest value for fractional anisotropy was found in the splenium of the corpus callosum, where $FA = 0.74$.

Within the simulations in Section 5, we will not make use of the EMA for the conductivity tensor eigenvalues as described in the introduction. We are rather interested in using conductivity tensors of the form $\sigma = \mathbf{S\Lambda S}^T$ with $\mathbf{S}$ the orthogonal matrix of eigenvectors of the measured diffusion tensors, but with simulated eigenvalues $\mathbf{\Lambda} = \text{diag}(\lambda_{long}, \lambda_{trans}, \lambda_{trans})$ as described in Table 2 in Subsection 5.1.1. λ_{long} is the eigenvalue parallel (longitudinal) and λ_{trans} perpendicular (transverse) to the fibre directions. Figure 9 shows a detail of the projection of the conductivity tensor ellipsoids $\sigma = \mathbf{S\Lambda S}^T$ with an eigenvalue choice of $\lambda_{long} = 0.65$ and $\lambda_{trans} = 0.065$ onto a coronal slice of the T1-MRI. The eigenvalue choice corresponds to the modeled anisotropy

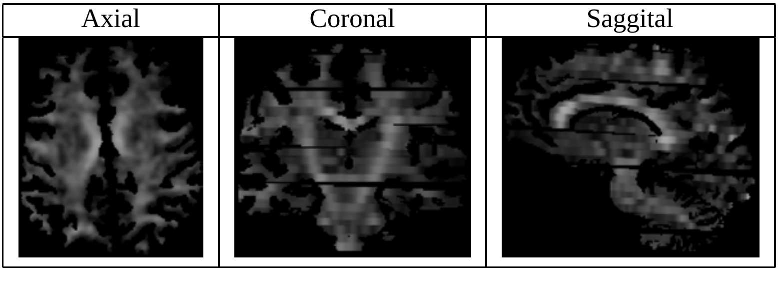

Fig. 8: Fractional anisotropy index, FA (see Equation 11), of the DT-MRI, masked with the white matter mask of the 5-tissue segmentation result.

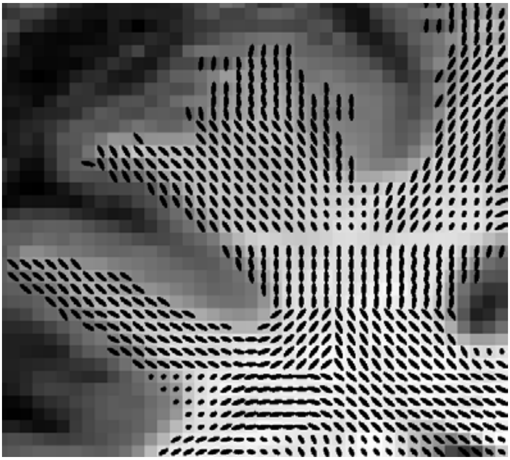

Fig. 9: Detail of the projection of the conductivity tensor ellipsoids σ onto a coronal cut of the T1-MRI through the Commissura anterior. The gap, where no measurement data was available, is not yet filled with isotropic conductivity tensors. Top right: Fibres going up to the Gyrus frontalis superior; top left: Fibres going up to the Gyrus frontalis medius; bottom right: Fibres going through the Truncus corporis callosi; bottom left: Fibres going up to the Gyrus precentralis and down to Gyrus frontalis inferior, pars opercularis. Tensor validation and visualization was carried out with the VM tool [SIMBIO, 2000].

ratio of 1:10 in Table 2 in Subsection 5.1.1. In Figure 9 the gap, where no measurement data was available, is not yet filled with isotropic conductivity tensors. The visualization of tensors in Figures 9, 10 and 11 was carried out with the software tool VM (Visualization Module), developed within the project [SimBio, 2000].

2.3 Meshing and discretization aspects

Numerical methods are needed for field simulations in realistically shaped anisotropic volume conductors. Within this article, we use the FE method.

2.3.1 FE mesh generation

An essential prerequisite for FE modeling is the generation of a mesh which represents the geometric and electric properties of the head volume conductor. Our approach uses a surface-based tetrahedral tessellation of the relevant compartments skin, skull, CSF, brain gray and white matter, and ventricular system, as described in [Wagner, 1998]. Auxiliary surfaces with a distance d_1 from the given compartment borders are generated so that a set of layered surfaces is obtained. In a next step, the vertices of the tetrahedral mesh are

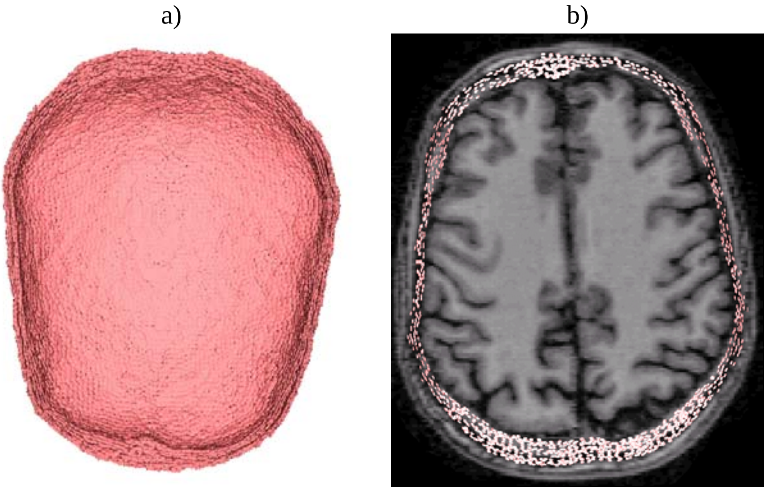

Fig. 10: Conductivity tensors in the barycenters of the skull elements for 1:5 anisotropy: a) Tensors of the skull roof. b) Tensors of an axial cut through the skull model on underlying T1-MRI. A stronger scaling of the eigenvalues of the tensors was chosen in a) compared to b). Tensor validation and visualization was carried out with the VM tool [SIMBIO, 2000].

Fig. 11: Conductivity tensor ellipsoids in the barycenters of white matter elements for 1:10 anisotropy on underlying T1-MRI: The eigenvalues were chosen as $\lambda_{long} = 0.65$ *and* $\lambda_{trans} = 0.065$ *according to Table 2 in Subsection 5.1.1. Tensor validation and visualization was carried out with the VM tool [SIMBIO, 2000].*

generated by means of a thinning of the surfaces with thinning-distance d_1 for auxiliary and d_2 for compartment surfaces. $d_2 = 2mm$ enabled a very exact representation of the volume conductor. A distance of 1.3 times d_2 was chosen for d_1. This resulted in 147287 nodes. After a three-dimensional Delaunay triangulation, each of the 892115 tetrahedra was labeled according to its compartment. The tetrahedral FE mesh was generated using the software package [CURRY, 2000].

According to the procedure described in 2.2.1, an anisotropic conductivity tensor was assigned to the barycentre of each finite element in the skull. Figure 10 shows the conductivity tensors of the skull roof (left) and of an axial cut through the skull model on underlying T1-MRI (right) for 1:5 anisotropy. Tensor validation and visualization was carried out with the VM tool [SimBio, 2000]. To the barycentre of each finite element in the white matter compartment, we assign the anisotropic conductivity tensor derived from the measured diffusion tensor image with $1mm^3$ resolution, presented in Subsection 2.2.2. Figure 11 shows the conductivity tensor ellipsoids in the barycenters of the white matter finite elements for 1:10 anisotropy on the underlying T1 MRI. Again, the tensors were validated and visualized by means of the VM tool [SimBio, 2000].

2.3.2 The blurred dipole model

A direct approach for the discretization of Equation (2) is used within this article. Therefore, the blurred dipole model was introduced for FE based source localization in [Buchner *et al.*, 1997], which will be shortly summarized below. The blurred dipole is made up from monopole sources $J_k^b := J^b(\vec{x}_k)$, calculated for all neighboring FE mesh nodes $\vec{x}_k$ around the location $\vec{x}_i$ of a mathematical dipole $\vec{M}_i := \vec{M}\delta(\vec{x} - \vec{x}_i)$, so that

$$\begin{aligned} F &= \frac{1}{2}\left({}^{n_0}\vec{M}_i^r - \left(\Delta\bar{\vec{x}}_{ki}^r\right)^{n_0} J_k^b\right)\left({}^{n_0}\vec{M}_i^r - \left(\Delta\bar{\vec{x}}_{si}^r\right)^{n_0} J_s^b\right) \\ &\quad +\lambda\frac{1}{2}J_k^b g_{ks} J_s^b \overset{!}{=} min \\ g_{ks} &:= \left\{ \begin{array}{cl} \left(\Delta\bar{\vec{x}}_{ki}^r \Delta\bar{\vec{x}}_{si}^r\right)^{n_s/2} & if\ k = s \\ 0 & if\ k \neq s \end{array} \right. \end{aligned}$$

with $\Delta\bar{\vec{x}}_{ki}^r = \Delta\vec{x}_{ki}^r/a$ the r cartesian component of the a-weighted vector from node i to node k, $\Delta\vec{x}_{ki}$, n_0 the order of the source model, n_s the dipole smoothness and λ the dipole regularization parameter. The first part of the functional F ensures a minimal difference between the resultant moment of the blurred dipole and the one of the mathematical dipole, while the second part, a Tikhonov-Phillips regularizer, smoothes the monopole distribution and enables a unique minimum for F. The differentiation of F with respect to $J^{\,b}$ is used to express the minimum condition which leads to a system of linear equations:

$$\begin{aligned}\left[\left(\Delta\bar{\vec{x}}^{r}_{ki}\right)^{n_0}\left(\Delta\bar{\vec{x}}^{r}_{si}\right)^{n_0}+\lambda g_{ks}\right]J_s^b &= \left(\Delta\bar{\vec{x}}^{r}_{ki}\right)^{n_0}\vec{M}_i^{n_0} \\ \sum_k J_k^b &= 0\end{aligned} \tag{12}$$

Together with $J_t^b = 0$ for all non-neighbor indices t of dipole index i, the monopole distribution of the blurred dipole model is defined. See [Buchner *et al.*, 1997] for a motivation of this source model and for accuracy tests in a sphere model, where the numerical results were compared with results of an analytical formula from [Smythe, 1989] for two closely neighbored monopoles, a source and a sink.

2.3.3 FE formulation for EEG forward computation

The direct application of variational and FE techniques to equation (2) with boundary conditions (3) together with the blurred dipole model yields a system of linear equations

$$\mathsf{K}_{h\,h} = \underline{\mathsf{J}}_h \tag{13}$$

with $\mathsf{K}_h \in \mathbb{R}^{N_h \times N_h}$ denoting the stiffness matrix, $\underline{\mathsf{J}}_h \in \mathbb{R}^{N_h}$ the source load and ${}_h \in \mathbb{R}^{N_h}$ the solution vector for the total potential. The stiffness matrix is given by

$$\mathsf{K}_h^{[i,j]} = \int_\Omega \nabla\psi_j \sigma \nabla\psi_i \, d\Omega \tag{14}$$

and the right hand side entries for the direct method by

$$[\underline{\mathsf{J}}_h]^i = -\int_\Omega J_i^b \psi_i \, d\Omega \tag{15}$$

for an FE space $\mathbb{V}_h = span\{\psi_i\}_{i=1}^{N_h}$. The subscript h denotes the average meshsize and $N_h = O(h^{-3})$ is the number of unknowns. The condition number of the stiffness matrix behaves asymptotically like $O(h^{-2})$.

In contrast to the described direct discretization method in combination with the blurred dipole model, the subtraction method (see e.g. [Awada *et al.*, 1997; van den Broek *et al.*, 1997; Schimpf *et al.*, 2002]) splits the total potential into two parts, the singularity potential and the correction potential. The singularity potential is the analytically calculated solution for a mathematical current dipole (equation (1)) in an unbounded homogeneous conductor with constant isotropic conductivity. The correction potential is a solution to equation 2 in the closed sourceless domain under boundary conditions that correct

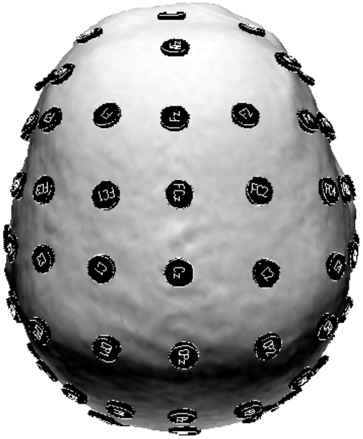

Fig. 12: EEG sensors: 71 electrodes of the chosen EEG system. Electrode size was enlarged for visualization purposes.

the movement of current across boundaries between regions of different conductivity. The correction potential is calculated by means of an FE approach, leading to a linear equation system with the same stiffness matrix (14), but with different right hand side. Since the solvers are independent of the right hand side of the equation system, the results presented in the following are also valid for the subtraction method in combination with the mathematical dipole.

For the EEG forward computation, 71 electrodes were placed interactively on the head surface according to the international 10/20 system [Pastelak-Price, 1983]. The electrode configuration is shown in Figure 12. The sensors were projected onto the FE head model, i.e., we model the electrode potential with the value of the closest neighboring FE mesh node.

2.3.4 MEG forward computation

For the magnetic forward problem, the flux transformers of the MEG device have to be modeled. The Max-Planck-Institute of Cognitive Neuroscience Leipzig is equipped with a BTI 148 channel whole-head MEG system. [Pohlmeier, 1996] modeled each coil Υ of this system (see Figure 13, left) by means of a thin, closed conductor loop with a diameter of 11.5 mm, using 8 isoparametric quadratic finite row elements. Errors slightly below the data noise between this realistic and a point-like coil representation were reported, showing the necessity of the chosen approach. With regard to these

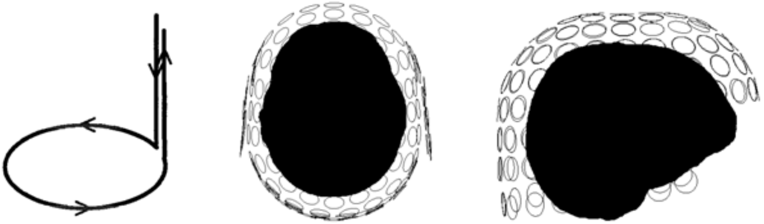

Fig. 13: MEG sensors: Magnetometer flux transformer (left) and the chosen whole head BTI-148-channel MEG system together with the FE head model, top view (middle) and side view (right).

results, equation (7) was discretized by means of

$$\vec{C}(\vec{y}) = \sum_{n} \int\limits_{-1}^{1} \frac{1}{|\sum\limits_{i(n)} \chi_i(\xi)\vec{x}_i - \vec{y}|} \sum_{i(n)} \frac{\partial \chi_i(\xi)}{\partial \xi} \vec{x}_i d\xi, \tag{16}$$

where n denotes a finite row element and an isoparametric FE Ansatz with quadratic (parabolic) Ansatz functions χ_i was made for the coil position vector, $\vec{x}(\xi) = \sum_i \chi_i(\xi)\vec{x}_i$, with $\vec{x}_i$ the vertices of the row element. The determination of the primary flux Ψ_p in Equation (8) is then straight-forward. After the FE calculation of the potential distribution, the secondary flux Ψ_s in Equation (9) is computed by means of a Gauss integration, where the integrand consists of the interpolated functions in the FE space [Pohlmeier, 1996]. In Figure 13, the position of the 148 magnetometer coils, each represented by its row elements, are visualized together with the FE head model.

3 Parallel Algebraic Multigrid Solver

The inverse reconstruction process requires the solution of hundreds or even thousands of large scale systems of equations (13) with the stiffness matrix (14). In [Wolters *et al.*, 2000], condition numbers of about 10^7 have been calculated for high resolution realistically shaped head stiffness matrices, causing severe accuracy and convergence problems for classical iterative solvers. These problems were recovered by applying appropriate preconditioners for the CG method such that the condition number of the resulting preconditioned stiffness matrix was small. The AMG preconditioner was shown to be superior to incomplete Cholesky factorization with threshold. In [Johnson *et al.*, 2000], AMG-CG was found to be superior to a successive overrelaxation method.

If we are going to solve the entire localization problem with many calls of the solver, the results cannot be produced within an acceptable time. However, a parallel computer may provide sufficient capacity such that time limitation can be fulfilled. In [Haase *et al.*, 2002; Wolters *et al.*, 2002] it has been shown that AMG-CG solvers exhibit high speedups on parallel computers including PC clusters and an SGI ORIGIN 2000. The speedup was especially good for the solver-part of the algorithm. Since the setup of the preconditioner has to be carried out only once per head geometry, its calculation time and speedup can be neglected. Our following description of the parallel AMG is taken from [Wolters *et al.*, 2002].

3.1 Algebraic Multigrid Method

As in Geometric MultiGrid (GMG, see [Hackbusch, 1985] for a theoretical overview), the basic idea in AMG is to reduce high and low frequency components of the error by the efficient interplay of smoothing and coarse grid correction, respectively. In AMG, both, the matrix hierarchy and the prolongation operators are constructed just from the stiffness matrix K_h. In analogy, we will speak of "coarse grids" although these are purely virtual and do not have to be constructed explicitly as coarse FE meshes. Since the automatic generation of a grid-hierarchy for GMG and especially the proper assembling of all components would be a very difficult task with respect to conductivity inhomogeneities and anisotropies in a realistically shaped head model, the automatic algebraic construction of a virtual grid is a big advantage. A general concept of AMG methods for FE discretizations can be found in [Haase *et al.*, 2000]. Each AMG algorithm consists of the following components:

(a)Coarsening: define the splitting $\omega_h = \omega_C \cup \omega_F$ of ω_h (the index set of nodes) into sets of coarse and fine grid nodes ω_C and ω_F, respectively.
(b)Transfer operators: prolongation $\mathfrak{P}_h : V_H \mapsto V_h$ and restriction $\mathfrak{R}_h := \mathfrak{P}_h^T$.
(c)Definition of the coarse matrix by Galerkin's method, i.e., $\mathsf{K}_H := \mathfrak{R}_h \mathsf{K}_h \mathfrak{P}_h$.
(d)Appropriate smoother for the considered problem class.

The most important issue to be discussed is the setup phase, i.e., the construction of the matrix hierarchy and the prolongation operators. We will give the explanation for a two grid method where h is related to the fine grid and H to the coarse grid.

In our case, the stiffness matrix K_h can be associated with an FE grid, i.e., the diagonal entry of the i^{th} row of the matrix K_h is related to a grid point in ω_h and an off-diagonal entry is related to an edge in an FE grid (see

Figure 14). First we look at the coarsening process which has the task to

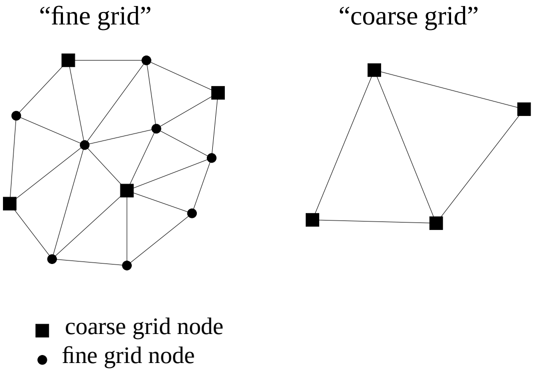

Fig. 14: Illustration of a two grid method.

reduce the nodes such that $N_H = |\omega_C| < N_h = |\omega_h|$. Here, $|\omega|$ denotes the number of elements in the set ω. Motivated from Figure 14, the grid points ω_h can be split into two disjoint subsets ω_C (coarse grid nodes) and ω_F (fine grid nodes), i.e.,

$$\omega_h = \omega_C \cup \omega_F, \quad \omega_C \cap \omega_F = \emptyset$$

such that there are (almost) no direct connections between any two coarse grid nodes and the resulting number of coarse grid nodes is as large as possible. Instead of considering all connections between nodes being of the same rank, we introduce the following sets

$$\begin{aligned} N_h^i &= \Big\{ j \mid |\mathsf{K}_h^{[i,j]}| \neq 0,\ i \neq j \Big\} \qquad (17) \\ S_h^i &= \Big\{ j \in N_h^i \mid |\mathsf{K}_h^{[i,j]}| > coarse(i,j,\mathsf{K}_h) \Big\} \\ S_h^{i,T} &= \Big\{ j \in N_h^i \mid i \in S_h^j) \Big\} \end{aligned}$$

where N_h^i is the index set of neighbors, S_h^i denotes the index set of nodes with a “strong connection” from node i and $S_h^{i,T}$ is related to the index set of nodes with a “strong connection” to node i (see [Ruge and Stüben, 1986]). In addition $coarse(i,j,\mathsf{K}_h)$ is an appropriate cut-off (coarsening) function, e.g.,

$$coarse(i,j,\mathsf{K}_h) := \alpha \cdot \max_j \{ |\mathsf{K}_h^{[i,j]}| \}\,, \qquad (18)$$

Algorithm 2 (Parallel) $V(\nu_F, \nu_B)$-cycle MG$(\mathsf{K}_h, , \underline{\mathsf{J}})$

```
if CoarseGrid then
    $\Leftarrow$ DirectSolve $(\mathsf{K} \cdot \;\; = \; \underline{\mathsf{J}})$
else
   $\tilde{}\Leftarrow$ $\nu_F$ times Smooth$(\mathsf{K}_h, , \underline{\mathsf{J}})$
   $\underline{\mathsf{d}} \leftarrow \underline{\mathsf{J}} - \mathsf{K}_h \cdot \tilde{}$
   $\underline{\mathsf{d}}^H \leftarrow \mathfrak{P}^T \cdot \underline{\mathsf{d}}$
   $\underline{\mathfrak{w}}^H \leftarrow 0$
   $\underline{\mathfrak{w}}^H \Leftarrow$ MG$(\mathsf{K}_H, \underline{\mathfrak{w}}^H, \underline{\mathsf{d}}^H)$
   $\underline{\mathfrak{w}} \leftarrow \mathfrak{P} \cdot \underline{\mathfrak{w}}^H$
   $\hat{}\leftarrow\tilde{}+ \underline{\mathfrak{w}}$
    $\Leftarrow$ $\nu_B$ times Smooth$^T(\mathsf{K}_h, \hat{}, \underline{\mathsf{J}})$
end if
```

with $\alpha \in [0, 1]$. With those definitions a splitting into coarse and fine grid nodes can be done. For our computations we used a modified splitting algorithm of [Ruge and Stüben, 1986]. Next the prolongation operator has to be defined correctly. We require that the prolongation operator $\mathfrak{P}_h : V_H \mapsto V_h$ has full rank. There are a lot of possibilities to define such transfer operators with pure algebraic information. For the construction we refer to [Ruge and Stüben, 1986; Braess, 1995; Kickinger, 1998; Wagner, 2000]. A possible setting and the one which turned out to be the most efficient for the presented application is given by

$$(\mathfrak{P}_h)^{[i,j]} = \begin{cases} 1 & i = j \in \omega_C \\ 1/|S_h^{i,T} \cap \omega_C| & i \in \omega_F,\ j \in S_h^{i,T} \cap \omega_C \\ 0 & \text{else}\,. \end{cases} \tag{19}$$

The coarse grid matrix K_H is defined by the classical Galerkin method, i.e.,

$$\mathsf{K}_H = \mathfrak{P}_h^T \mathsf{K}_h \mathfrak{P}_h \in \mathbb{R}^{N_H \times N_H},$$

being again symmetric and positive definite (see e.g. [Ruge and Stüben, 1986]).

After the proper definition of the prolongation and coarse grid operators a matrix hierarchy can be setup in a recursive way. Finally, a multigrid cycle can be assembled, see Algorithm 2. Therein the variable COARSEGRID denotes the level where a direct solver is applied.

For our application we use AMG-CG, i.e., AMG is applied as a preconditioner for the CG method (see [Jung and Langer, 1991]). For the m-$V(\nu_F, \nu_B)$-cycle AMG preconditioned CG method, the operation $\underline{\mathfrak{w}} =$

Algorithm 3 (Par.) PCG algorithm PCG($\mathsf{K}_h, , \underline{\mathsf{J}}, \mathsf{C}_K$)

```
$\underline{\mathsf{r}} \leftarrow \underline{\mathsf{J}} - \mathsf{K}_h$
$\underline{\mathfrak{w}} \Leftarrow \mathsf{C}_K^{-1} \cdot \underline{\mathsf{r}}$
$\underline{\mathfrak{s}} \leftarrow \underline{\mathfrak{w}}$
$\gamma \Leftarrow \langle \underline{\mathfrak{w}}, \underline{\mathsf{r}} \rangle$
repeat
    $\underline{\mathsf{v}} \leftarrow \mathsf{K}_h \cdot \underline{\mathfrak{s}}$
    $\alpha \Leftarrow \gamma / \langle \underline{\mathfrak{s}}, \underline{\mathsf{v}} \rangle$
    $\leftarrow + \alpha \underline{\mathfrak{s}}$
    $\underline{\mathsf{r}} \leftarrow \underline{\mathsf{r}} - \alpha \underline{\mathsf{v}}$
    $\underline{\mathfrak{w}} \Leftarrow \mathsf{C}_K^{-1} \cdot \underline{\mathsf{r}}$
    $\gamma \Leftarrow \langle \underline{\mathfrak{w}}, \underline{\mathsf{r}} \rangle$
    $\beta \leftarrow \gamma / \gamma_{\text{OLD}}$ , $\gamma_{\text{OLD}} \leftarrow \gamma$
    $\underline{\mathfrak{s}} \leftarrow \underline{\mathfrak{w}} + \beta \underline{\mathfrak{s}}$
until TERMINATION
```

$\mathsf{C}_K^{-1}\underline{\mathsf{r}}$ is realized by m calls of MG($\mathsf{K}_h, \underline{\mathfrak{w}}, \underline{\mathsf{r}}$). For the Jacobi-preconditioner, it is $\mathsf{C}_K = \mathsf{D}$ with D the diagonal of K_h. The Preconditioned CG (PCG) method is shown in Algorithm 3.

3.2 Data Partitioning

The aim of parallelization is to split both data and operations to the P processors available. The consistency of the algorithms is preserved by message passing. In our case, the parallelization is based on a non-overlapping domain decomposition, i.e., we decompose $\overline{\Omega}$ into P subdomains $\overline{\Omega}_s$ such that

$$\overline{\Omega} = \bigcup_{s=1}^{P} \overline{\Omega}_s$$

with

$$\Omega_s \cap \Omega_q = \emptyset \quad \forall q \neq s, \quad s, q = 1, \ldots, P$$

holds. Each subdomain Ω_s is discretized by a mesh $\tau_{h,s}$ such that the whole triangulation

$$\tau_h = \bigcup_{s=1}^{P} \tau_{h,s}$$

of Ω forms a conforming mesh. A global FE space $\mathbb{V}_h$ is defined with respect to τ_h and the local spaces $\mathbb{V}_{h,s}$ are restrictions of $\mathbb{V}_h$ onto $\tau_{h,s}$.

The mesh partitioning of realistic FE geometries with unstructured meshes is critical for the efficiency of the parallel solver method. The distribution

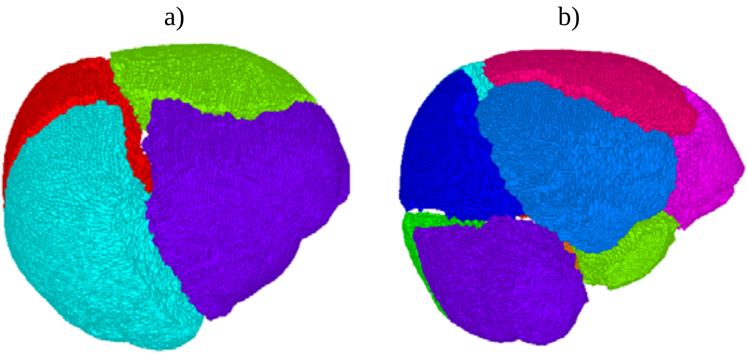

Fig. 15: Realistic tetrahedral FE head model, 892115 elements, partitioned with METIS and visualized with PMVIS: a) for 4 processors b) for 12 processors.

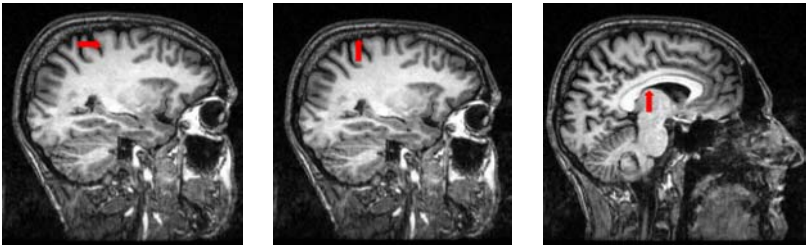

Fig. 16: Simulated sources on underlying T1-MRI: Almost tangentially oriented somatosensory source (left), somatosensory source with large radial orientation component (middle) and left thalamic source (right).

must be done so that the number of elements assigned to each processor is the same and the number of adjacent elements assigned to different processors is minimized in order to balance the computation amount among the processors and to minimize the communication between them, respectively. Therefore, graph partitioning algorithms were used which model the FE mesh by a graph (V, E) with vertices V and edges E. Since we are interested in an "element-wise-" in contrast to a "node-wise-" distribution, the dual graph of the FE mesh was partitioned. The finite elements are the vertices of the dual graph and adjacent elements are the corresponding edges. A balanced k-way partitioning was used, minimizing the number of edges which straddle partitions. No weighting of the edges, e.g. with regard to jumping conductivities between elements at tissue-boundaries, was used. The algorithm is based on a multilevel approach, first reducing the size of the dual graph by collapsing vertices and edges, then partitioning the dual graph on the lowest level and further refine during the uncoarsening steps. For the described mesh-partitioning, the software package METIS was used [Karypis and Kumar, 1998]. The results were achieved in a few seconds on a single processor SGI workstation. A first examination of the partitioning result was carried out by means of zooming, rotating, translating, scaling, and applying explosion factors. Figure 15 shows a visualization of the partitioned geometries for 12 processors (see [Öztekin *et al.*, 1998]). Later, the number of interface and inner nodes and the number of elements were controlled during the calculations. The interface nodes are those nodes which belong to at least two processors, whereas inner nodes only belong to one. In all cases, the quality of the partitioning results were very satisfactory.

3.3 Parallel AMG

The mapping of a vector $\underline{\Phi}_h \in \mathbb{R}^{N_h}$ in global numbering onto a local vector $\underline{\Phi}_s \in \mathbb{R}^{N_s}$ in subdomain $\overline{\Omega}_s$ $(s = 1, \ldots, P)$ is represented symbolically by subdomain connectivity matrices $\mathcal{A}_s : \mathbb{R}^{N_h} \mapsto \mathbb{R}^{N_s}$ with entries

$$\mathcal{A}_s^{[i,j]} := \begin{cases} 1 & \text{if} \quad j = \textsc{Loc2Glob}(i) \\ 0 & \text{else} \end{cases} \qquad \forall i \in \omega_s \, , \; \forall j \in \omega_h$$

where $\textsc{Loc2Glob}(\cdot)$ maps a local index to the global index. The transpose $\mathcal{A}_s^T$ of these binary matrices $\mathcal{A}_s$ maps a local vector back onto the global one. The index set of all those subdomains to which an unknown $\Phi_h^{[j]}$, $j \in \omega_h$ belongs, is denoted by

$$\sigma^{[j]} := \{ s \mid \Phi_h^{[j]} \in \overline{\Omega}_s \} \, . \tag{20}$$

We store the data related to the i^{th} node in the subdomain Ω_s if $s \in \sigma^{[i]}$. This approach results in local data denoted by index s of two types [Haase, 1999]: *accumulated data* (vector , matrix $\mathfrak{P}$) represented by

$$_s \;:=\; \mathcal{A}_s \cdot \;\;, \qquad \mathfrak{P}_s \;:=\; \mathcal{A}_s \cdot \mathfrak{P} \cdot \mathcal{A}_s^T \tag{21}$$

and *distributed data* (vector $\underline{\mathsf{d}}$, matrix K_h) represented by

$$\underline{\mathsf{d}} \;=\; \sum_{s=1}^{P} \mathcal{A}_s^T \cdot \underline{\mathsf{d}}_s, \qquad \mathsf{K}_h \;:=\; \sum_{s=1}^{P} \mathcal{A}_s^T \cdot \mathsf{K}_s \cdot \mathcal{A}_s\,. \tag{22}$$

It turns out, that in Algorithms 2 and 3, the functionals are represented as distributed data ($\underline{\mathsf{J}}$, $\underline{\mathsf{v}}$, $\underline{\mathsf{r}}$, $\underline{\mathsf{d}}$, K_h), whereas functions are represented as accumulated data (, $\underline{\mathfrak{s}}$, $\underline{\mathfrak{w}}$, $\mathfrak{P}$). The local FE accumulation with respect to $\mathbb{V}_{h,s}$ produces automatically distributed matrices K_s. For instance, it can be shown that the multiplication of a distributed matrix K_h with the accumulated vector $\underline{\mathfrak{s}}$ in Algorithm 3 results in a distributed vector $\underline{\mathsf{v}}$:

$$\begin{aligned} \mathsf{K}_h \cdot \underline{\mathfrak{s}} = \; & \sum_{s=1}^{P} \mathcal{A}_s^T \mathsf{K}_s \mathcal{A}_s \cdot \underline{\mathfrak{s}} \;=\; \sum_{s=1}^{P} \mathcal{A}_s^T \left(\mathsf{K}_s \cdot \underline{\mathfrak{s}}_s\right) \\ = \; & \sum_{s=1}^{P} \mathcal{A}_s^T \underline{\mathsf{v}}_s \;=\; \underline{\mathsf{v}} \end{aligned}$$

The realization requires no communication at all because we only have to compute $\underline{\mathsf{v}}_s = \mathsf{K}_s \cdot \underline{\mathfrak{s}}_s$ locally.

If an accumulated matrix $\mathfrak{M}$ fulfills the condition

$$\forall i \in \omega_h\,, \forall j \in \omega_C \;:\; \sigma^{[i]} \not\subseteq \sigma^{[j]} \implies \mathfrak{M}^{[i,j]} = 0, \tag{23}$$

then the operations $\underline{\mathfrak{w}} \;=\; \mathfrak{M} \cdot \underline{\mathfrak{w}}^H$, $\underline{\mathsf{d}}^H \;=\; \mathfrak{M}^T \cdot \underline{\mathsf{d}}$ and $\mathsf{K}_H = \mathfrak{M}^T \mathsf{K}_h \mathfrak{M}$ can be performed locally without any communication [Haase, 1999].

In AMG the coarsening and prolongation operators are components which can be chosen. The main idea in the design of parallel AMG is to choose these components such that the resulting prolongation operators $\mathfrak{P}$ are of accumulated type satisfying the pattern condition (23). For this purpose, a local node ordering is introduced by means of a grouping and ordering of the index sets (20) according to $|\sigma^{[j]}|$. The coarsening then starts at interfaces involving more than 2 processors and continues with faces between two processors and finally the coarsening of inner nodes is realized. In addition the coarsening has to be synchronized such that the coarse grid problem is conforming across interfaces between processors. This synchronization requires next neighbor communication. Note that the partitioning of the nodes has only been performed on the finest grid. For a detailed discussion we refer to [Haase *et al.*, 2002].

Now we observe that Algorithm 2 and Algorithm 3 are also the appropriate parallel formulations, where double-line arrows "$\Leftarrow$" indicate that communication is required for the corresponding operation. In Algorithm 2, the coarse grid system is accumulated globally once in the setup phase. During the iteration only a vector has to be assembled for computing the coarse grid solution. Furthermore, the smoother requires communication and has to be adapted appropriately. We use a Gauss-Seidel smoother for the inner nodes and a Jacobi smoother for the interface nodes. The Jacobi-smoother involves a vector conversion from distributed to accumulated type, i.e., one next neighbor communication across interfaces is required per smoothing step. In this way we get a sophisticated smoother which can be found in [Haase, 1999]. In Algorithm 3, only inner products involve communication besides the preconditioning operation. Since for the inner product of different type vectors it is

$$\begin{aligned}\langle \underline{\mathfrak{w}}, \underline{\mathfrak{r}} \rangle &= \underline{\mathfrak{w}}^T \sum_{s=1}^{P} \mathcal{A}_s^T \underline{\mathfrak{r}}_s = \sum_{s=1}^{P} \left(\mathcal{A}_s \underline{\mathfrak{w}}\right)^T \underline{\mathfrak{r}}_s \\ &= \sum_{s=1}^{P} \langle \underline{\mathfrak{w}}_s, \underline{\mathfrak{r}}_s \rangle ,\end{aligned}$$

only one global reduce operation is needed.

4 Software developments

A new FE software package NeuroFEM was developed, based on the package CAUCHY (see [CAUCHY, 1997; Buchner *et al.*, 1997]). Since it would have been difficult to integrate the FORTRAN77-CAUCHY code using quasistatic memory management in a new C++ class structured inverse toolbox, the old software was redesigned. The inverse toolbox contains a variety of state-of-the-art current source localization methods ([SimBio, 2000], see also [Knösche, 1997; Wolters *et al.*, 1999a]). Another argument for the code development was the possibility for a proper interface to the software package PEBBLES including the parallel AMG solver ([Reitzinger, 1999; Haase *et al.*, 2002]). The solver code exploits C++ principles of overloading and inheritance.

Therefore, C++ class structured software concepts replace old CAUCHY kernel routines. The storage management within NeuroFEM is fully dynamical so that a recompilation of the software is no longer necessary when changing the problem- and thus memory- size. The new structure facilitated parallel programming on distributed memory computers using the Message-Passing Interface (MPI) standard. The integrated software allows future comparisons with Boundary Element (BE) method based forward simulations (see e.g.[Zanow and Peters, 1995; Fuchs *et al.*, 1998]) or series expansion formulas in spherical shell models [de Munck and Peters, 1993].

The coupling to the parallel solver-package is carried out through an "element by element" interface. The root-process determines the index set (20) for each node of the partitioned geometry and scatters the corresponding data together with the conductivity tensors to the processors. The arrangement of the nodes to groups according to their index-sets, the ordering of the groups and the allocation of corresponding MPI-communicator groups and the local node numbering is then a fully parallel process. Element-stiffness-matrices are computed on each processor and stored in the local stiffness matrices in FE compact row format. These matrices automatically have the distributed data format (22). The global Dirichlet-node information is scattered to all processors and implemented with a penalty approach in local numbering to those local stiffness matrices whose processor-number is part of the global Dirichlet-node index-set. The coarsening can then be carried out and the hierarchy of stiffness and prolongation matrices can be determined in the parallel setup-phase of the AMG preconditioner as described in Section 3.

5 Results and discussion

After discussion of parameter settings and definition of sensitivity error measures, we present simulation results concerning the influence of tissue conductivity anisotropy on EEG and MEG for typical current sources in the brain. Performance results of the parallel AMG solver and its sensitivity to tissue anisotropy will be discussed in the last part of the section.

5.1 Parameter settings and error measures

5.1.1 Simulated sources

Simulation studies were carried out with three blurred dipolar current sources at two different locations in the brain (see Figure 16 before p. 134). The first two sources, one of them almost tangentially oriented (in y-direction, Figure 16, left) and the other radially (in z-direction, Figure 16, middle), were chosen in the right somatosensory cortex as an example for eccentric, i.e., superficial sources. The second location was chosen in the left thalamus as an example for deeper sources, where the orientation is always almost radial (Figure 16, right). For the parameters of the blurred dipoles (see equation

(12)), we chose $n_0 = 2$ for the order of the source model, $n_s = 2$ for the dipole smoothness, $\lambda = 10^{-6}$ for the regularization parameter and $a = 20.0$ for the dipole scale, effecting a spatial concentration of monopole loads J_k in the dipole axis around the dipole node. This choice also led to best results in sphere model accuracy tests, when comparing the numerical results with an analytical formula from [Smythe, 1989] for two closely neighboring monopoles, a source and a sink, see [Buchner *et al.*, 1997].

5.1.2 Volume conductor modeling

	Volume constraint		Wang's constraint	
$\lambda_{rad} : \lambda_{tang}$	λ_{rad}	λ_{tang}	λ_{rad}	λ_{tang}
1:1 (iso)	0.0042	0.0042	0.0042	0.0042
1:2	0.0026	0.0053	0.003	0.0058
1:5	0.00143	0.0072	0.00188	0.00938
1:10	0.000905	0.00905	0.00133	0.01326
1:100	0.000195	0.0195	0.00042	0.042

Tab. 1: Skull conductivity tensor eigenvalue settings: λ_{rad} is the conductivity tensor eigenvalue for radial and λ_{tang} for tangential direction.

The conductivity σ of the chosen isotropic skin- and grey matter-elements was set to 0.33 1/Ωm. An isotropic conductivity value of 1.79 1/Ωm was assigned to elements in the CSF [Baumann *et al.*, 1997], i.e., within the compartment between brain and skull and within the ventricular system. The conductivity tensor eigenvectors of skull elements were determined by means of the procedure, described in Subsection 2.2.1. The conductivity eigenvalues for an isotropic skull layer were set to 0.0042 1/Ωm, resulting in the well-known conductivity ratio of about $1 : 80$ between skull and skin layer (see, e.g., [Haueisen, 1996]). For a chosen anisotropy ratio, $\lambda_{rad} : \lambda_{tang}$, radial ($\lambda_{rad}$) and tangential ($\lambda_{tang}$) eigenvalues were calculated, obeying two different constraints: The first constraint, namely retaining $\lambda_{rad} \cdot \lambda_{tang}$ between the isotropic and anisotropic models, was proposed in [Wang *et al.*, 2001; van den Broek, 1997]. Our second constraint tries to retain the geometric mean of the eigenvalues and thus the volume of the conductivity tensor, $4/3\pi\lambda_{rad}\lambda_{tang}^2$. Table 1 shows the 5 chosen anisotropy ratios and the calculated eigenvalues under constraint of the respective approach. We chose anisotropy ratios of $1 : 2$, $1 : 5$, $1 : 10$ and $1 : 100$, where the last should be considered to be out of the realistic range. For the white matter compartment, the eigenvectors of a measured water diffusion tensor at the barycentre of a white matter finite element were taken as its conductivity tensor eigenvectors. The conductivity eigenvalues for an isotropic white matter compartment

	Volume method		Wang's method	
$\lambda_{trans} : \lambda_{long}$	λ_{trans}	λ_{long}	λ_{trans}	λ_{long}
1:1 (iso)	0.14	0.14	0.14	0.14
1:2	0.111	0.222	0.099	0.19798
1:5	0.0818	0.41	0.0626	0.31309
1:10	0.065	0.65	0.04427	0.4427
1:100	0.03016	3.016	0.014	1.4

Tab. 2: White matter conductivity tensor eigenvalue settings: λ_{long} is the conductivity tensor eigenvalue for longitudinal and λ_{trans} for transverse fibre direction.

were set to 0.14 1/Ωm (see, e.g., [Haueisen, 1996]). The anisotropy of the white matter compartment was varied through a variation of the eigenvalues assigned to the longitudinal fibre direction (parallel to white matter fibre bundles, i.e., the eigenvector direction with the largest eigenvalue in the water diffusion tensor), λ_{long}, and transverse direction, λ_{trans}, again obeying the two constraints which were described above. Table 2 shows the chosen anisotropy ratio, $\lambda_{trans} : \lambda_{long}$, and the resulting eigenvalues. Again, we chose the anisotropy ratios $1:2$, $1:5$, $1:10$ and $1:100$, where the last should again be considered to be out of the realistic range.

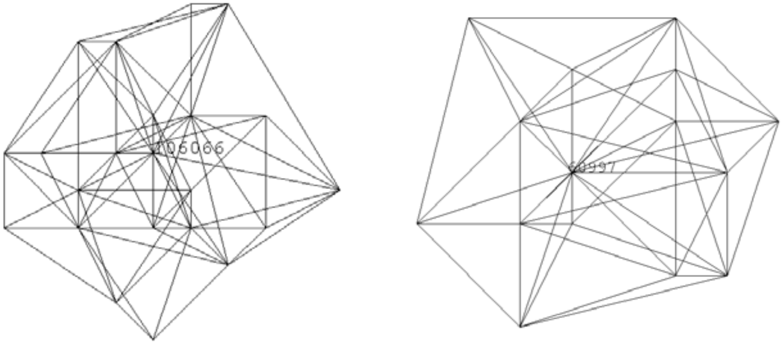

Fig. 17: Determined 41 finite elements in the neighborhood of the eccentric source at vertex 106066 (left) and the 29 neighbored finite elements of the deep source at vertex 60997 (right).

In [Haueisen *et al.*, 2000], a strong influence of local conductivity changes around the source location to EEG and MEG was reported. Therefore, in our model with 1:10 anisotropy of white matter and skull (volume constraint), we first determined 41 finite elements in the neighborhood around the eccentric source, 5 of which were isotropic CSF, 30 isotropic grey matter and 6 anisotropic white matter elements (Fig. 17, left). To the latter 6 elements, we then assigned the isotropic white matter conductivity. This model is denoted by EALC (Eccentric 1:10 Anisotropic Locally Changed). For the deep source, we determined 29 neighbored finite elements (Fig. 17, right), all of which were anisotropic white matter elements. The isotropic white matter conductivity tensor was then assigned to these elements, resulting in the DALC (Deep 1:10 Anisotropic Locally Changed) model.

5.1.3 Settings for the FE solution process

The zero starting vector $\Phi_0 = \vec{0}$ was chosen for the iterative solution process. The FE space $\mathbb{V}_h$ consisted of piecewise linear Ansatz-functions. Note that the solver-speed of the algorithms in Section 3 is only dependent on the stiffness matrix (14), so that the following results are valid for both the direct and the subtraction method (see Subsections 2.1 and 2.3.3) and all possible source configurations (i.e., independence of the right-hand side of the linear equation system). For the AMG-CG, we used the 1-$V(1,1)$-cycle AMG-preconditioner. Equation (18) was taken as the cut-off coarsening function with $\alpha = 0.01$ and the prolongation was chosen as in (19), respecting the pattern condition (23). The factorization in Algorithm 2 was carried out, if the size of the coarsest grid (COARSEGRID) in the preconditioner-setup was below 800. The coarse system is solved by means of a Cholesky-factorization. We observed only a small influence of the coarse grid size towards the solver times, when, e.g., increasing from COARSEGRID=800 to 1000.

The process of determining the index set (20) for each node and scattering the data to the processors, both of which are carried out by the root processor, and the local arrangement of nodes to groups according to their index-set and the allocation of corresponding communicator groups takes about half a minute. This duration can be neglected since these processes have to be performed only once per head model.

The solver process was stopped after the i^{th} iteration if the relative error in the controllable $\mathsf{K}_h\mathsf{C}_K^{-1}\mathsf{K}_h$-energy norm was below $\epsilon = 10^{-8}$, i.e.,

$$\frac{\langle \underline{\mathfrak{w}}^i, \underline{\mathsf{r}}^i \rangle}{\langle \underline{\mathfrak{w}}^0, \underline{\mathsf{r}}^0 \rangle} \leq \epsilon^2.$$

The simulations were run on an SGI ORIGIN 2000 with R10000, 195 MHz processors and overall 6GB of main memory. The solver speedup for 1 up to 12 processors was investigated.

5.1.4 Error criteria for sensitivity determination

We now define the two error criteria, which shall describe the influence of skull and white matter anisotropy on the field distribution. These criteria were introduced for Boundary Element calculations in [Meijs *et al.*, 1989]. The first error criterion, the Relative Difference Measure (RDM) at M measurement sensors, defined as

$$\mathrm{RDM} = \sqrt{\sum_{n=1}^{M} \left(\frac{\Phi_n^{iso}}{\sqrt{\sum_{n=1}^{M} \left(\Phi_n^{iso}\right)^2}} - \frac{\Phi_n^{aniso}}{\sqrt{\sum_{n=1}^{M} \left(\Phi_n^{aniso}\right)^2}} \right)^2}, \qquad (24)$$

is a measure for the topography error (Optimum RDM $= 0$). The second error measure, the MAGnification factor (MAG), defined as

$$\mathrm{MAG} = \frac{\sqrt{\sum_{n=1}^{M} \left(\Phi_n^{aniso}\right)^2}}{\sqrt{\sum_{n=1}^{M} \left(\Phi_n^{iso}\right)^2}}, \qquad (25)$$

gives an indication of errors in the magnitude.

5.2 Influence of tissue conductivity anisotropy on EEG and MEG

5.2.1 Results for a tangentially oriented eccentric source

Forward calculations for the eccentric source with a large tangential orientation component (Figure 16, left) and a strength of 10 nAm were carried out in the 5-tissue model and the sensitivity of EEG and MEG towards anisotropy of the skull layer, the white matter compartment, and of both skull and white matter was determined. Figure 18 shows the resulting RDM (left) and MAG (right) errors for an increasing anisotropy ratio, when either obeying the volume constraint or Wang's constraint.

Our EEG results concerning 1:10 anisotropic skull in combination with an isotropic white matter compartment are generally in agreement with the observations in [Marin *et al.*, 1998], where a topography error of about 10% and a magnification factor larger than 1 was reported for an eccentric tangentially oriented dipole in a realistic FE head model. However, [Marin *et al.*, 1998] modeled 1:10 skull anisotropy by fixing the radial and increasing the tangential conductivity eigenvalues by a factor of 10. If we do so, we observe a much larger topography error (RDM=20%) and a much larger magnification factor (MAG=1.72) (see also Figure 19, bottom row, right). This difference could be attributed to different simulation parameters like skull thickness and source location, and to the definition/evaluation of RDM and MAG. [Marin *et al.*, 1998] evaluated an integral over the whole head surface, whereas we considered only the potentials at the 71 EEG electrodes. We focus on the influence of anisotropy on the inverse EEG problem, where in practice, only

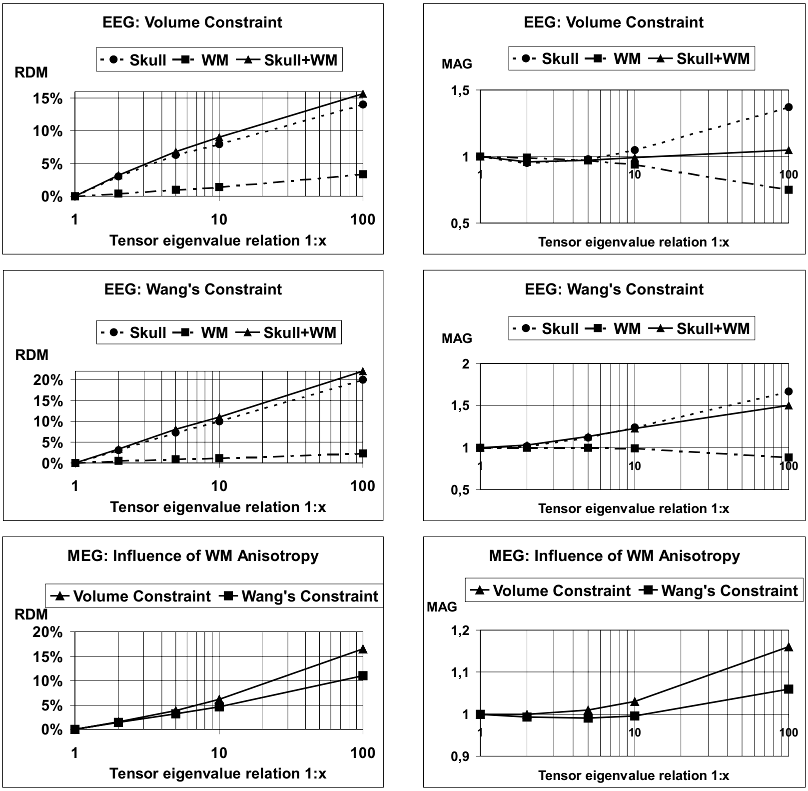

Fig. 18: Eccentric source, large tangential orientation component: EEG/MEG topography error (left) and magnitude error (right) for different anisotropy ratios: For EEG, errors due to anisotropy effects of skull, white matter (WM) and both skull and WM are presented for the tensor volume retaining (top row) and Wang's constraint [Wang et al., 2001] (middle row). For MEG, only WM anisotropy effects for both constraints are presented, since skull anisotropy was found to have no influence.

a limited number of sensors is available. The electrodes are often placed around the "center of interest" in order to sample the whole measurable dipolar pattern (see Figure 4). Figure 19 shows the isopotential distribution of the somatosensory source interpolated on the head surface of various FE forward calculations in the 5-tissue model. The isopotential distribution for the isotropic skull layer is shown in Figure 19, top row, left, and the result for 1:10 anisotropy with volume constraint in Figure 19, top row, right. The two 1:10 skull anisotropy isopotential distributions, presented in the bottom row of Figure 19, were calculated either by means of a fixation of the tangential

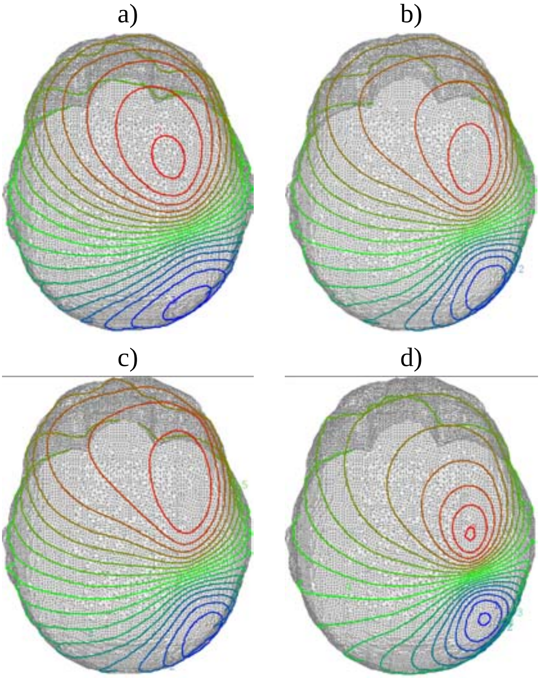

Fig. 19: Topography of isopotential distribution of the eccentric source with large tangential orientation component on upper part of the head a) isotropic skull ($\lambda_{rad} = 0.0042$*,* $\lambda_{tang} = 0.0042$*); from -0.9 to 0.2* μV *b) 1:10 anisotropic skull; volume method:* $\lambda_{rad} = 0.000905$ *and* $\lambda_{tang} = 0.00905$*); from -1.1 to 0.3* μV *c) 1:10 anisotropic skull; 10 times lower radial cond.:* $\lambda_{rad} = 0.00042$ *and* $\lambda_{tang} = 0.0042$*; from -0.7 to 0.1* μV *d) 1:10 anisotropic skull; 10 times higher tangential cond.:* $\lambda_{rad} = 0.0042$ *and* $\lambda_{tang} = 0.042$*; from -2.2 to 0.9* μV*.*

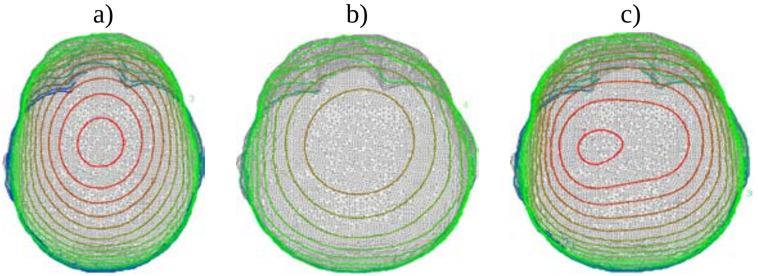

Fig. 20: Thalamic source: Isopotential distribution from -0.6 to 0.4 μV *on upper part of the head a) isotropic model:* $\lambda_{rad} = 0.0042$*,* $\lambda_{tang} = 0.0042$ *and* $\lambda_{trans} = 0.14$*,* $\lambda_{long} = 0.14$*. b) 1:10 anisotropic white matter (volume constraint):* $\lambda_{trans} = 0.065$ *and* $\lambda_{long} = 0.65$*; isotropic skull. c) 1:10 anisotropic skull (volume constraint):* $\lambda_{rad} = 0.000905$ *and* $\lambda_{tang} = 0.00905$*); isotropic white matter.*

conductivity eigenvalues and a reduction of the radial conductivity eigenvalue by a factor of 10 (left) or by means of a fixation of the radial conductivity eigenvalue and an increase of the tangential conductivity eigenvalues by a factor of 10 (right).

When comparing our results on skull anisotropy in realistic FE models with anisotropy examinations on multilayered sphere models [Zhou and van Oosterom, 1992; Marin *et al.*, 1998], we find the important difference that the EEG topography error between isotropic and 1:10 anisotropic skull modeling in our realistic FE head model (in agreement with the realistic FE head model in [Marin *et al.*, 1998]) is much larger than the EEG topography error between isotropic and 1:10 anisotropic spherical layer modeling, reported in [Zhou and van Oosterom, 1992; Marin *et al.*, 1998]. Additionally, a MAG close to 1 was pointed out for the spherical model [Zhou and van Oosterom, 1992], whereas for the realistic FE model, we found a MAG larger 1, like [Marin *et al.*, 1998]. Spherical symmetry effects could thus play a role, reducing topography and magnitude errors for the multilayered sphere model. However, these errors seem to be apparent in realistically shaped head models.

1:10 skull anisotropy was found to have no influence (RDM $< 1\%$, MAG ≈ 1) on the MEG topography and magnitude for both volume and Wang's constraint. This is in agreement with the generally accepted idea that volume currents in the skull and scalp layer give negligible contributions to the magnetic field [Hämäläinen and Sarvas, 1987] and with results in realistic FE head models [van den Broek *et al.*, 1997].

Our observations regarding the influence of white matter anisotropy on EEG/MEG for an isotropic skull layer agree well with the results in [Haueisen *et al.*, 2002]. [Haueisen *et al.*, 2002] reported small topography and magnitude errors for EEG and MEG for an eccentric source with large tangential orientation component. We observed a negligible influence for a ratio of 1:10 on the EEG topography with an RDM close to 1% and on the MEG topography with an RDM of about 5%. Our observed MAG is close to the optimum in the realistic anisotropy range for both EEG and MEG (see Figure 18).

We computed EEG and MEG in the EALC model (see definition in 5.1.2) and compared these forward solutions to the corresponding model with 1:10 anisotropy of white matter and skull (volume constraint). For both EEG and MEG, an RDM smaller than 1% and a MAG of about 1 was found.

In summary, for the EEG, 1:10 anisotropy of both skull and white matter layer, leads to a topography error of about 9% for the volume constraint and 11% for Wang's constraint. The topography error is mainly due to skull anisotropy, whereas white matter anisotropy has only a small influence on the potential distribution for the chosen eccentric source with large tangential orientation component. When choosing the volume constraint, the magnitude error MAG for 1:10 anisotropy of skull and white matter layer is kept close to the optimum of 1.0, whereas Wang's constraint leads to a MAG of 1.23. An increase of radial or tangential skull conductivity contracts (in Figure 19, compare top row, left with bottom row, right), whereas a decrease spreads out the isopotential distribution on the surface. The pattern is also distorted (in Figure 19, compare top row, left with bottom row, left), so that an approximation of skull anisotropy effects by means of an increase or a decrease of the scalar isotropic skull conductivity value in BE head models seems to be impossible. This is in particular true, because further computations with different source locations and orientations showed that contraction or spreading out depends on parameters such as location/orientation of the source and skull shape and thickness (not shown).

For the MEG, no influence of skull anisotropy was observed. The influence of white matter was small for realistic anisotropy ratios.

5.2.2 Results for a radially oriented eccentric source

Forward calculations for the eccentric source with large radial orientation component (Figure 16, middle) and a strength of 10 nAm were carried out in the 5-tissue model. Figure 21 shows the resulting RDM (left) and MAG (right) errors for EEG and MEG.

1:10 realistic white matter anisotropy for a radially oriented eccentric source has a strong influence on the topography of EEG and MEG, a result which again mainly agrees with the results in [Haueisen *et al.*, 2002]. [Haueisen *et al.*, 2002] reported a large topography error for both EEG and MEG (our MEG results have to be compared to the flux density component B_y in Table 2 in [Haueisen *et al.*, 2002]) and a moderate magnitude error for an eccentric almost radially oriented source. We observed an EEG topography error of RDM=23% for the volume and RDM=20% for Wang's constraint and an MEG topography error of about 15% for both constraints. The large MEG topography error can be explained by the fact that white matter anisotropy influences the secondary (return) currents and that the ratio of the secondary to the whole magnetic flux increases with increasing ratio of the radial dipole orientation component [Haueisen *et al.*, 1995]. Remember that for radially oriented sources in spherical head models, the primary magnetic flux (and because of spherical symmetry effects also the secondary magnetic flux) is zero outside the model. For both EEG and MEG, the MAG was again close to the optimum 1.0 for realistic white matter anisotropy ratios except for the MEG in combination with the volume constraint, where the error was close to 1.1.

We again found an RDM smaller than 1% and a MAG of about 1 between forward results in the EALC (see 5.1.2) and the corresponding locally unchanged model for both EEG and MEG.

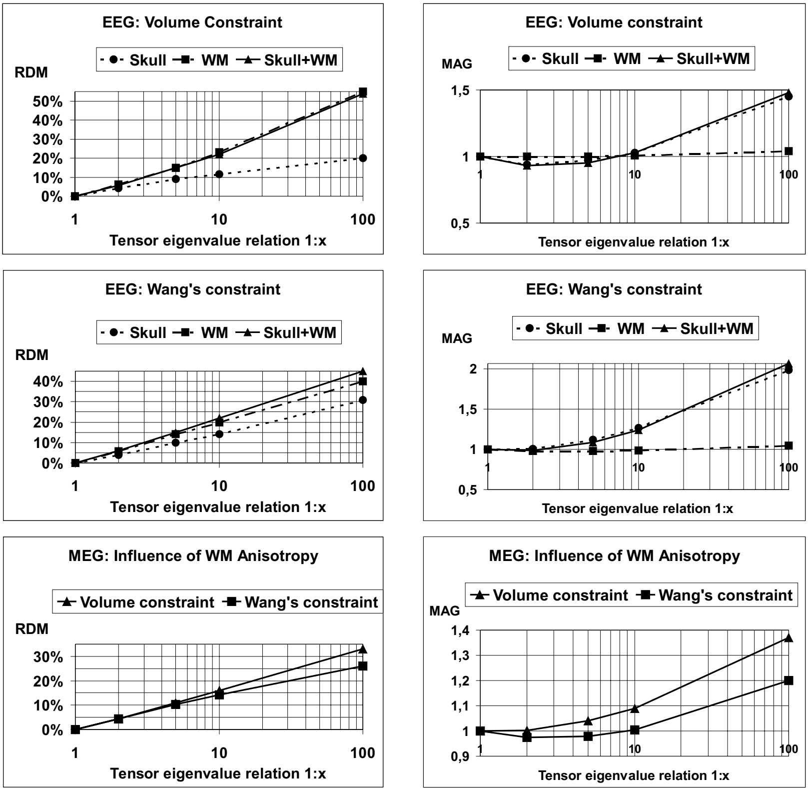

Fig. 21: Eccentric source, large radial orientation component: EEG/MEG topography error (left) and magnitude error (right) for different anisotropy ratios: For EEG, errors due to anisotropy effects of skull, white matter (WM) and both skull and WM are presented for the tensor volume retaining (top row) and Wang's constraint [Wang et al., 2001] (middle row). For MEG, only WM anisotropy effects for both constraints are presented, since skull anisotropy was found to have no influence.

Our EEG results concerning 1:10 anisotropy of the skull agree well with the observations in [Marin *et al.*, 1998]. With an RDM of 12% for the volume and 14% for Wang's constraint, the influence on the potential topography is in the range as seen for the tangential dipole. We achieved a MAG close to 1 for the volume and a MAG of 1.27 for Wang's constraint. For MEG, as for the tangential eccentric source, no influence (RDM $<$ 1%, MAG $\approx$ 1) of skull anisotropy was found (see [Hämäläinen and Sarvas, 1987], [van den Broek *et al.*, 1997]).

In summary, 1:10 anisotropy of both considered compartments leads to

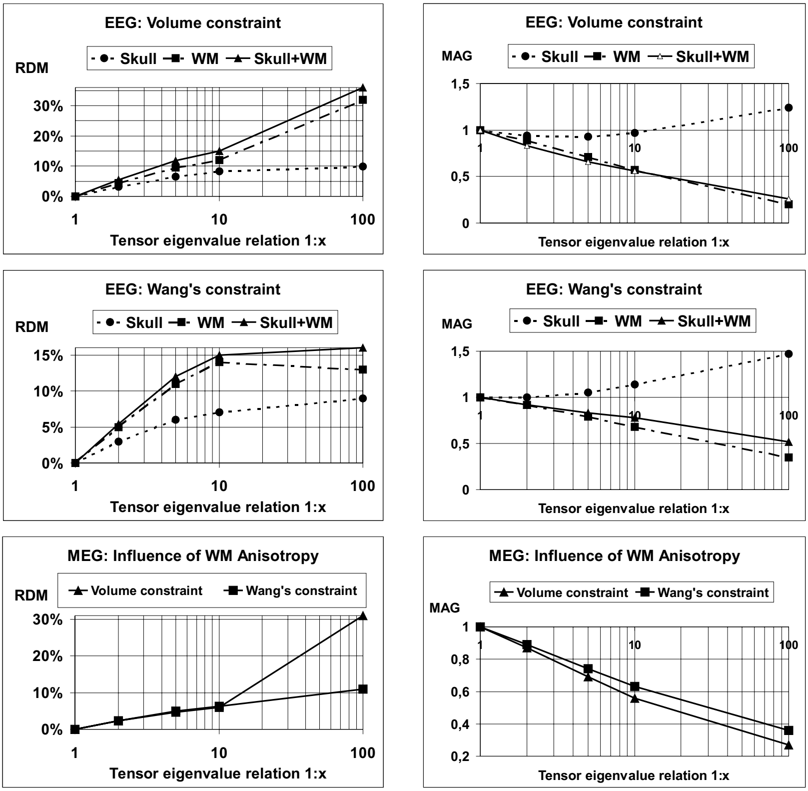

Fig. 22: Deep thalamic source: EEG/MEG topography error (left) and magnitude error (right) for different anisotropy ratios: For EEG, errors due to anisotropy effects of skull, white matter (WM) and both skull and WM are presented for the tensor volume retaining (top row) and Wang's constraint [Wang et al., 2001] (middle row). For MEG, only WM anisotropy effects for both constraints are presented, since skull anisotropy was found to have no influence.

a non-negligible topography error for both EEG and MEG. This error is mainly due to white matter anisotropy. Skull anisotropy has no influence on the MEG, but a non-negligible influence on the EEG. For EEG, the volume constraint led to a smaller MAG error than Wang's constraint, whereas we observed the inverse for the MEG. The local change from anisotropic to isotropic conductivity of white matter elements in the neighborhood of the source did not influence our error considerations.

5.2.3 Results for a deep source

In a last simulation, forward calculations in the 5-tissue-model were carried out for a deep and thus almost radial source (Figure 16, right) with a strength of 10 nAm. In the thalamus, tissue structure is almost radially oriented. Figure 22 shows the resulting RDM and MAG errors. Figure 20 (before p. 143) shows the isopotential distribution of the thalamic source for three different volume conductor models. The isopotentials for the isotropic 5-tissue model are shown on the left. In the middle, we present the result for an isotropic skull layer and a 1:10 anisotropic white matter compartment (volume constraint) and on the right the result for 1:10 anisotropic skull (volume constraint) and isotropic white matter compartment.

It can be observed from the Figs. 22 and 20, that 1:10 anisotropy of white matter in combination with an isotropic skull layer leads to a non-negligible topography error larger 10% for the EEG, whereas with 6%, the error is moderate for the MEG, but it is then strongly increasing for larger anisotropy ratios. White matter anisotropy strongly decreased the surface potential (Figure 20, middle, and MAG=0.57 in Figure 22, top row, right) and the magnetic fields (MAG$\approx$0.6 in Figure 22, bottom row). The former is related to the results of [Zhou and van Oosterom, 1992], who reported a decreased (increased) potential magnitude for increased (decreased) radial conductivity in the inner sphere of a multilayer sphere model, whereas for a change in the tangential conductivity component, no influence was found.

When comparing forward computation results between DALC (see definition in 5.1.2) and the corresponding locally unchanged model, we found an RDM of 16% and a MAG of 1.34 for the EEG and an RDM of 14% and a MAG of 1.19 for the MEG. In contrast to the eccentric source, these results show the importance of local conductivity changes, as reported by [Haueisen *et al.*, 2000].

For EEG, we observed an RDM of about 7% for 1:10 anisotropic skull in combination with an isotropic white matter compartment (Figure 22 and Figure 20, right) and an increase in the magnitude for Wang's constraint (Figure 22, middle row, right, MAG = 1.14), while the magnitude was kept close to the optimum for the volume constraint (Figure 22, top row, right, MAG = 0.97). For the MEG, we only observed a small influence (RDM $<$ 3%, MAG=0.98) for Wang's constraint (not shown).

In summary, for the deep thalamic source, a non-negligible influence of 1:10 skull and white matter anisotropy on the EEG topography was found. The EEG topography error is mainly due to white matter, but to a minor extent also to skull anisotropy. For the MEG, we assume that white matter anisotropy has a non-negligible influence on the topography, whereas skull anisotropy can be neglected. White matter anisotropy strongly reduced EEG and MEG field magnitude. Local conductivity changes were strongly influencing our error considerations.

5.3 Performance results and sensitivity of the FE solution process towards tissue conductivity anisotropy

In [Wolters *et al.*, 2002], nearly linear speedups of the parallel AMG method were reported for high resolution realistically shaped isotropic tetrahedra and cube head models. In comparison to a classical parallel Jacobi preconditioned conjugate gradient method, large improvements in the computation time were found for the parallel AMG. In the following, the performance of both solver methods will be examined for the high resolution realistically shaped anisotropic tetrahedra model in comparison to the corresponding isotropic one. The stability of both preconditioners with regard to realistic tissue anisotropy will be analysed.

5.3.1 The isotropic tetrahedra model

We first discuss the FE solution process within the isotropic tetrahedra model. We chose the deep thalamic source. The local accumulation of the geometry matrix K_s on 1 processor took 225 seconds, parallelized on 12 processors a setup time of 19 seconds was achieved.

Figure 23 shows the wall-clock time of the parallel AMG-CG solver compared to the parallel Jacobi-CG. The number of iterations for both solvers, necessary for the required accuracy, is shown over the curves. The time for the setup of the preconditioner is not included, since it has to be carried out only once per head model and is thus negligible with regard to the solution of the inverse problem. To give an impression, the setup of the AMG on 1 processor took 39 seconds and parallelized on 12 processors 7.6 seconds. The 3D potential distribution was calculated on one processor within 370 seconds with the Jacobi-CG method, whereas the parallel AMG-CG method on 10 processors needed 4.2 seconds. This is a factor of about 88 (10.2 through multigrid preconditioning and 8.6 through parallelization on 10 processors).

The speedup results from 1 to 12 processors are shown in Figure 24. The matrix generation is purely local and gives the reference curve for the quasi optimal speedup. This curve can also be seen as an indicator for the quality of the mesh-partitioning, described in Subsection 3.2. The speedups for the parallel AMG-CG solver, for one iteration of this solver and for the parallel Jacobi-CG solver are compared.

Since the coarsening process and the determination of the prolongation matrix $\mathfrak{P}$ respecting pattern condition (23) in the setup of the parallel AMG-preconditioner and the smoother-component of the solver depend on the de-

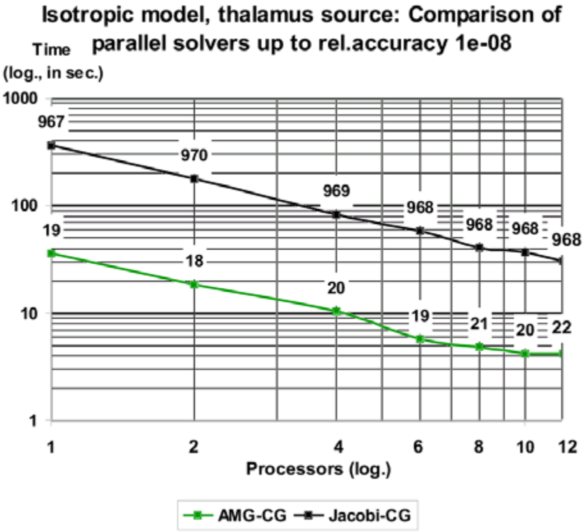

Fig. 23: SGI ORIGIN: Wall-clock time from 1 to 12 processors for the solver part of the parallel AMG-CG compared to the parallel Jacobi-CG up to an accuracy of 10^{-8} *for the realistic tetrahedra head model, 147287 nodes and a dipole source in the thalamus. The number of iterations are shown over the curves.*

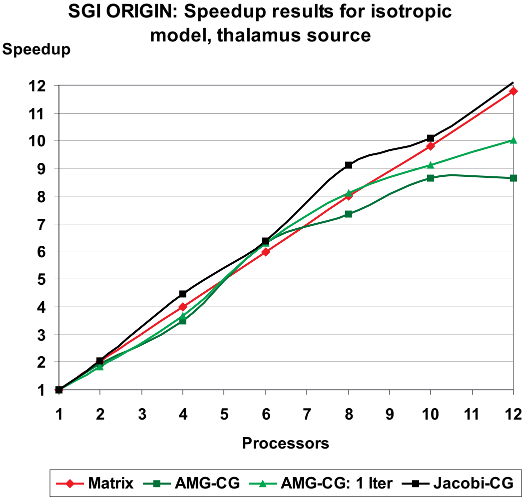

Fig. 24: SGI ORIGIN: Speedup results from 1 to 12 processors for the tetrahedra head model, 147287 nodes and a deep thalamic source.

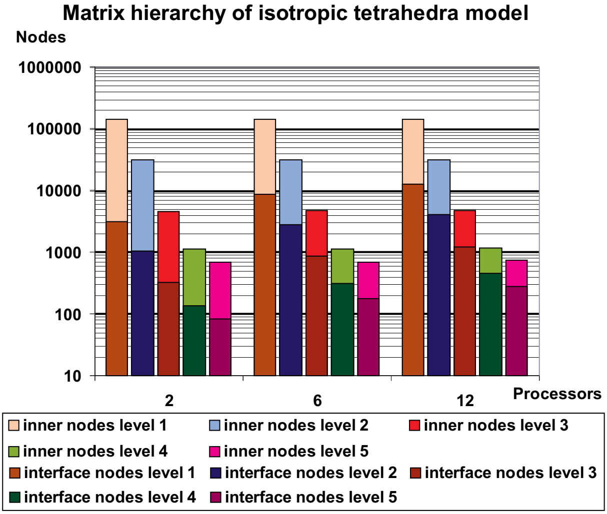

Fig. 25: Isotropic tetrahedra head model, 147287 nodes: Relation interface nodes to all nodes (interface plus inner nodes) on the four levels of the algebraic multigrid, exemplarily for the decompositions for 2, 6 and 12 processors.

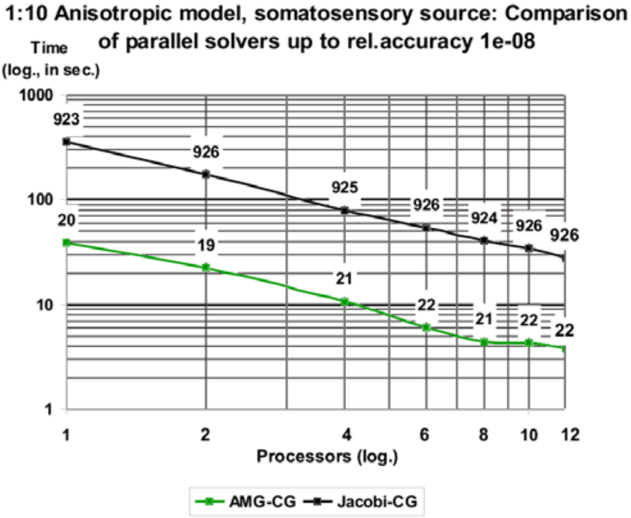

Fig. 26: SGI ORIGIN: Wall-clock time from 1 to 12 processors for the solver part of the parallel AMG-CG compared to the parallel Jacobi-CG up to an accuracy of 10^{-8} for 1:10 anisotropic tetrahedra head model, 147287 nodes and the almost tangentially oriented eccentric source. The numbers of iterations are shown over the curves.

composition into subdomains and a strongly increasing number of interface-nodes would spoil the preconditioning effect, it is interesting to have a look at the relation of interface nodes to all nodes (interface plus inner nodes) on the different levels of the multigrid. Figure 25 shows this relation exemplarily for 2, 6 and 12 processors. The decomposition into two domains lead to 3084 and thus 2% interface nodes on the finest level. On the fourth level (their is no more smoother component on the fifth and coarsest virtual grid), 133 out of 1117 nodes were interface nodes and thus a percentage of 12%. On 12 processors, 12462 and thus 8% were interface nodes on the finest level and on the fourth level, 461 out of 1164, i.e., 40%. In summary, it can be concluded that the results are close to what we found for the isotropic tetrahedra head model in [Wolters *et al.*, 2002].

5.3.2 1:10 anisotropic tetrahedra model

We now discuss the solution process for the potential distribution within the anisotropic tetrahedra model with 1:10 anisotropic skull and white matter layer for the tangentially oriented eccentric source. The accumulation of the local geometry matrices on 1 and parallelized on 12 processors takes the same times as it was presented for the isotropic model above.

Figure 26 shows the wall-clock time of the parallel AMG-CG solver compared to the parallel Jacobi-CG for the anisotropic model. Again, the number of iterations is shown over the curves. As for the isotropic model, the time for the setup of the preconditioner is not included. The setup of the AMG on 1 processor took 39 seconds and parallelized on 12 processors 7 seconds in the anisotropic case. The 3D potential distribution was calculated on one processor within 361 seconds with the Jacobi-CG method, whereas the parallel AMG-CG method on 12 processors needed 3.8 seconds. This is a factor of about 95 (9.3 through multigrid preconditioning and 10.2 through parallelization on 12 processors).

In [Wolters *et al.*, 2000], condition numbers of high resolution 4 layer sphere FE models were computed. No remarkable difference between isotropic models and models with 1:10 anisotropic third (“skull”) layer were reported. It was observed, that the anisotropy lead to a slight increase of Jacobi iterations, whereas the iteration count of the AMG-CG was constant. For the realistic tetrahedra head model, we now observe the inverse behavior, a slight decrease of Jacobi-CG iterations (967 for the isotropic and 923 for the anisotropic) and a slight increase of AMG-CG iterations (19 for the isotropic and 20 for the anisotropic case). If we expect that the condition numbers of isotropic and anisotropic models are again in the same range, we explain the slight changes of the iteration count to be in the range of $O(1)$. Remember also that different sources were chosen for the isotropic and the anisotropic model. The speedup results from 1 to 12 processors are shown in Figure 27. Again, the matrix generation gives the reference curve for the quasi optimal speedup.

It is also interesting to consider the number of interface nodes as a fraction of all nodes on the five levels of the multigrid. Figure 28 shows these node numbers for 2, 6 and 12 processors. The decomposition into two domains lead to 3084 and thus again 2% interface nodes on the finest level. On the 4^{th} level, 120 out of 1022 nodes were interface nodes and thus a percentage of 12%. On 12 processors, 12462 and thus 8% were interface nodes on the finest level and on the fourth level, 443 out of 1066, i.e., 42%.

6 Conclusions

Head tissue conductivity anisotropy has a non-negligible influence on the EEG/MEG field distribution and should therefore be taken into account. These findings in our article are in agreement with results of [van den Broek *et al.*, 1997; Marin *et al.*, 1998; Haueisen *et al.*, 2002]. We presented non-invasive measurement techniques and image processing methods for obtaining a high resolution anisotropic map of the two tissue compartments skull and white matter. For solving the EEG/MEG inverse problem, the field distribution has to be simulated repeatedly for given dipolar sources in the brain. The chosen modern numerical approach in combination with high performance computing on a parallel machine was shown to yield computation times, which should push high resolution realistically shaped anisotropic forward modeling within the EEG/MEG inverse problem into the application fields.

Our presented head model was constructed from an MRI segmentation of the five tissue compartments skin, skull, cerebrospinal fluid and brain grey and white matter. The modeling of skull anisotropy was based on results for an improved segmentation of inner and outer skull surfaces, using bimodal MRI data. Realistic skull conductivity tensors were obtained by means of the surface normals of a smooth surface spongiosa model, for which the segmentation results of inner and outer skull were exploited. Whole head DT-MRI measurements were used to determine the conductivity tensor eigenvectors for each point in the white matter compartment. The diffusion tensor eigenvector with largest measured eigenvalue was taken for modeling the high conductive longitudinal white matter fibre direction.

Boundary element method based volume conductor models (see, e.g., [Fuchs *et al.*, 1998; Zanow and Peters, 1995]) cannot take tissue conductivity anisotropy into account. In multilayered sphere models [de Munck and Peters, 1993; Zhou and van Oosterom, 1992], anisotropy of the inner spherical

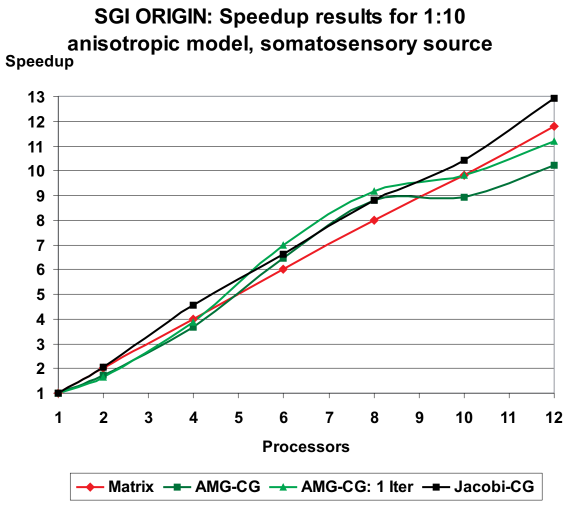

Fig. 27: SGI ORIGIN: Speedup results for 1:10 anisotropic tetrahedra head model and the almost tangentially oriented eccentric source, 147287 nodes, relative accuracy 10^{-8}.

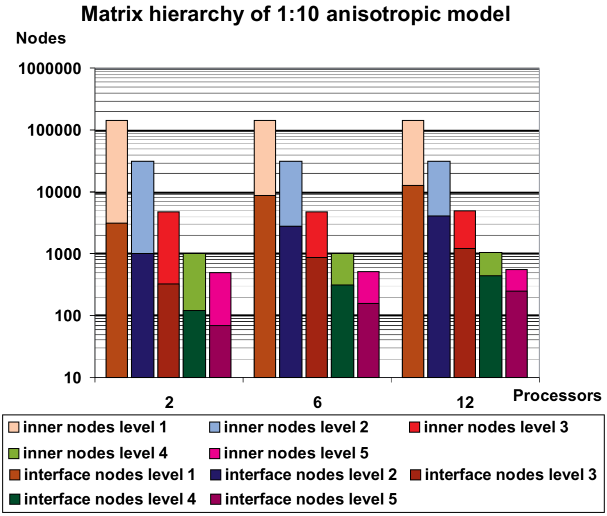

Fig. 28: 1:10 anisotropic tetrahedra head model, 147287 nodes: Relation interface nodes to all nodes (interface plus inner nodes) on the five levels of the algebraic multigrid, exemplarily for the decompositions for 2, 6 and 12 processors.

“white matter compartment” can only be represented by a single tensor, which is not realistic. We used high resolution realistic finite element head modeling, where a measured or realistically modeled tensor-valued conductivity was assigned to each finite element in the skull and white matter compartment. In order to test the influence of tissue anisotropy on EEG and MEG, different anisotropy ratios were modeled, following a constraint, proposed in [Wang *et al.*, 2001], and a tensor volume retaining constraint for achieving the desired ratio.

For the EEG, our influence results agree to a large extent with [van den Broek *et al.*, 1997; Marin *et al.*, 1998; Haueisen *et al.*, 2002]. For a tangentially oriented eccentric source, we found a topography error of about 10% between the isotropic and a 1:10 anisotropic model. The errors are mainly due to the skull, whereas we found that white matter anisotropy was negligible. The magnitude error for the volume retaining constraint was close to the optimum, whereas with increasing anisotropy ratio, it increased for Wang’s constraint. An increase of radial or tangential skull conductivity contracts, whereas a decrease spreads out the isopotential distribution on the surface. The isopotential pattern is also distorted, so that an approximation of skull anisotropy effects by means of an increase or a decrease of a scalar isotropic skull conductivity value in boundary element head models seems to be impossible. Thus, dipole mislocalizations have to be expected for tangentially oriented eccentric sources, if skull layer anisotropy is not taken into account.

For a radially oriented eccentric source, we found an EEG topography error of more than 20% between the isotropic and a 1:10 anisotropic model. In this case, the topography errors are mainly due to white matter anisotropy, the error of the skull layer was only about half the one of the white matter compartment. The magnitude error for the volume retaining constraint was again close to the optimum, while, again, it was larger for Wang’s constraint. A change of the local conductivities in the neighborhood of the eccentric source did not influence our error considerations. Larger dipole mislocalizations thus have to be expected for radially oriented eccentric sources if white matter or skull anisotropy is not taken into account.

For a deep source, we found an EEG topography error of about 15%, mainly due to white matter, but to a smaller extent also to skull layer anisotropy. White matter anisotropy strongly reduced the magnitude of the surface potential. A change of the local conductivities in the neighborhood of the deep source strongly influenced our error considerations, which is in agreement with results of [Haueisen *et al.*, 2000]. Larger dipole mislocalizations and errors in dipole strength estimations have to be expected for deeper sources if white matter or skull anisotropy is not taken into account..

We conclude that for robust EEG-based dipole source reconstruction in the human brain, tissue conductivity anisotropy of the skull as well as the white matter compartment has to be taken into account so that high resolution FE head modeling is needed.

We found, that skull anisotropy has no influence on the MEG, which is in agreement with the results of [van den Broek *et al.*, 1997] and with the generally accepted idea that volume currents in the skull and scalp layer give negligible contributions to the magnetic field [Hämäläinen and Sarvas, 1987]. In contrast to the skull compartment, white matter anisotropy was found to have a non-negligible influence on the MEG. In agreement with [Haueisen *et al.*, 2002], the topography error was moderate for an eccentric source with almost tangential orientation (about 5% for a ratio of 1:10), whereas it was much larger for an eccentric source with almost radial orientation (about 15%). The larger error can be explained by the fact that tissue anisotropy only influences the secondary (return) currents and that the ratio of the secondary to the whole magnetic flux increases with increasing ratio of the radial dipole orientation component [Haueisen *et al.*, 1995]. As for the EEG, a change of the local conductivities in the neighborhood of the eccentric source did not influence the error considerations. The magnitude error was again close to the optimum for both eccentric sources. For the deep source, in particular the magnitude error was large (MAG of about 0.6 for a ratio of 1:10), and from our results we also deduce that the topography error is not negligible. A change of the local conductivities in the neighborhood of the deep source strongly influenced the MEG error considerations, which is in agreement with results of [Haueisen *et al.*, 2000]. For MEG we conclude that white matter conductivity anisotropy has to be taken into account, if sources with a non-negligible radial orientation component should be reconstructed or if statements about the strength of deeper sources have to be made.

The bottleneck for a broader application of finite element method based anisotropic forward modeling is the time for solving the large linear equation system with thousands of different right hand sides arising from the FE discretization. Within this article, an efficient and memory-economical way was presented to face this problem. Very short calculation times were achieved through the combination of AMG preconditioning techniques and its parallelization on distributed memory platforms. We compared the presented AMG-CG with the Jacobi-CG, the latter being a well-known solver method in FE-based source localization. Our findings with regard to anisotropic head modeling strongly agree with the results in isotropic volume conductors [Wolters *et al.*, 2002]. If the Jacobi-CG on a single processor is taken as a reference, we achieved a speedup of 95 for a realistically shaped high resolution 1:10 anisotropic tetrahedra head model with 147287 nodes when comparing to the parallel AMG-CG on 12 processors, 9.3 through multigrid preconditioning and 10.2 through parallelization on 12 processors. The solver process was thus shown to be stable with respect to realistic tissue anisotropy.

The partitioning of the dual graph of a convex head geometry generally leads to a relatively large percentage of interface nodes. Nevertheless, for the examined moderate processor numbers between 1 and 12, the AMG-preconditioner was found to be stable, i.e., a sensible increase of the number of subdomains did not result in a deterioration of the AMG-preconditioner and thus an increasing need for iterations. We showed that the latter is true both for the isotropic and for the anisotropic model.

The presented methods and software concepts provide higher accuracy in EEG/MEG source localization by accounting for tissue conductivity anisotropy on the basis of a high resolution realistically shaped FE head model. Our methods allow the study of the influence of anisotropy on the inverse source localization results, where many forward solutions have to be computed. This will be done in future examinations. A first performance test of the NeuroFEM software on a Linux PC-cluster with 100 MBit ethernet showed very good parallelization speedups and, because of the 1 GB processors, a strongly reduced computation time compared to the presented results on the SGI ORIGIN 2000. The presented algorithms can thus be used on a simple PC-cluster. Moreover, the overall solver CPU-time for the inverse source reconstruction will be accelerated through the use of techniques for multiple right hand sides [Chan and Wan, 1997; Haase and Reitzinger, 2002]. First studies on a sequential computer have shown a good performance.

References

[Akhtari *et al.*, 2000] M. Akhtari, H.C. Bryant, A.N. Marmelak, L. Heller, J.J. Shih, M. Mandelkern, A. Matlachov, D.M. Ranken, E.D. Best, and W.W. Sutherling. Conductivities of three-layer human skull. *Brain Top.*, 13(1):29–42, 2000.

[Alexander *et al.*, 2001] D.C. Alexander, C. Pierpaoli, P.J. Basser, and J.C. Gee. Spatial transformations of diffusion tensor magnetic resonance images. *IEEE Trans. Biomed. Eng.*, 20(11):1131–1139, 2001.

[Andrä and Nowak, 1998] W. Andrä and H. Nowak. *Magnetism in medicine – a handbook*. Wiley–VCH, 1998.

[Awada *et al.*, 1997] K.A. Awada, D.R. Jackson, J.T. Williams, D.R. Wilton, S.B. Baumann, and A.C. Papanicolaou. Computational aspects of finite element modeling in EEG source localization. *IEEE Trans. Biomed. Eng.*, 44(8):736–751, 1997.

[Basser and Pierpaoli, 1996] P.J. Basser and C. Pierpaoli. Microstructural and physiological features of tissues elucidated by quantitive-diffusion-tensor MRI. *J. Magn. Reson. B*, 111:209–219, 1996.

[Basser *et al.*, 1994a] P.J. Basser, J. Mattiello, and D. LeBihan. Estimation of the effective self-diffusion tensor from the NMR spin echo. *J. Magn. Reson. B*, 103:247–254, 1994.

[Basser *et al.*, 1994b] P.J. Basser, J. Mattiello, and D. LeBihan. MR diffusion tensor spectroscopy and imaging. *Biophysical Journal*, 66:259–267, 1994.

[Bastian *et al.*, 1997] P. Bastian, K. Birken, K. Johannsen, S. Lang, N. Neuss, H. Rentz-Reichert, and C. Wieners. UG – A flexible Software Toolbox for Solving Partial Differential Equations. *Comput. Vis. Sci.*, 1:27 – 40, 1997.

[Baumann *et al.*, 1997] S.B. Baumann, D.R. Wozny, S.K. Kelly, and F.M. Meno. The electrical conductivity of human cerebrospinal fluid at body temperature. *IEEE Trans. Biomed. Eng.*, 44(3):220–223, 1997.

[Bertrand *et al.*, 1991] O. Bertrand, M. Thévenet, and F. Perrin. 3D finite element method in brain electrical activity studies. In J. Nenonen, H.M. Rajala, and T. Katila, editors, *Biomagnetic Localization and 3D Modelling*, pages 154–171. Report of the Department of Technical Physics, Helsinki Univ. of Technology, 1991.

[Braess, 1995] D. Braess. Towards algebraic multigrid for elliptic problems of second order. *Computing*, 55:379–393, 1995.

[Buchner *et al.*, 1997] H. Buchner, G. Knoll, M. Fuchs, A. Rienäcker, R. Beckmann, M. Wagner, J. Silny, and J. Pesch. Inverse localization of electric dipole current sources in finite element models of the human head. *Electroenc. Clin. Neurophysiol.*, 102:267–278, 1997.

[Burkhardt *et al.*, 2002] S. Burkhardt, C.H. Wolters, and D. Saupe. Segmentation of human skull surfaces from bimodal MRI volumes. 2002. submitted to Med.Imag.Anal.

[CAUCHY, 1997] CAUCHY. Anatomic source reconstruction of EEG/MEG-data. http://www.rwth-aachen.de/ neurologie/, 1997.

[Chan and Wan, 1997] T.F. Chan and W. L. Wan. Analysis of projection methods for solving linear systems with multiple right-hand sides. *SIAM J. Sci. Comput.*, 18(6):1698 – 1721, 1997.

[CURRY, 2000] CURRY. Current reconstruction and imaging. NeuroScan Labs, http://www.neuro.com/ neuroscan/ prod05.htm, 2000.

[de Munck and Peters, 1993] J.C. de Munck and M. Peters. A fast method to compute the potential in the multi sphere model. *IEEE Trans. Biomed. Eng.*, 40(11):1166–1174, 1993.

[de Munck *et al.*, 1988] J.C. de Munck, B.W. van Dijk, and H. Spekreijse. Mathematical dipoles are adequate to describe realistic generators of human brain activity. *IEEE Trans. Biomed. Eng.*, 35(11):960–966, 1988.

[Falgout *et al.*, 1999] R. Falgout, Van E. Henson, J. E. Jones, and U. Meier Yang. Boomer AMG: A parallel implementation of algebraic multigrid. Techn. Report UCRL-MI-133583, Lawrence Livermore National Laboratory, March 1999.

[Fuchs *et al.*, 1998] M. Fuchs, M. Wagner, H.A. Wischmann, T. Köhler, A. Theißen, R. Drenckhahn, and H. Buchner. Improving source reconstructions by combining bioelectric and biomagnetic data. *Electroenc. Clin. Neurophysiol.*, 107:93–111, 1998.

[Gueziec and Hummel, 1994] A. Gueziec and R. Hummel. The wrapper algorithm: surface extraction and simplification. In *IEEE Workshop on Biomedical Image Analysis, Seattle*, pages 204–213. IEEE Computer Press, Los Alamitos, 1994.

[Haase and Reitzinger, 2002] G. Haase and S. Reitzinger. Cache issues of algebraic multigrid methods for linear systems with multiple right-hand sides. Technical Report 02-05, J. Kepler Univ. Linz, SFB “Numerical and Symbolic Scientific Computing”, 2002.

[Haase *et al.*, 2000] G. Haase, U. Langer, S. Reitzinger, and J. Schöberl. A general approach to algebraic multigrid. Technical Report 00-33, J. Kepler Univ. Linz, SFB “Numerical and Symbolic Scientific Computing”, 2000.

[Haase *et al.*, 2002] G. Haase, M. Kuhn, and S. Reitzinger. Parallel AMG on distributed memory computers. *SIAM J. Sci.Comp.*, 2002. in press.

[Haase, 1999] G. Haase. *Parallelisierung numerischer Algorithmen für partielle Differentialgleichungen*. Teubner, 1999.

[Hackbusch, 1985] W. Hackbusch. *Multigrid Methods and Application*. Springer Verlag, 1985.

[Hämäläinen and Sarvas, 1987] M.S. Hämäläinen and J. Sarvas. Feasibility of the homogeneous head model in the interpretation of neuromagnetic fields. *Phys.Med.Biol.*, 32:91–97, 1987.

[Haueisen *et al.*, 1995] J. Haueisen, C. Ramon, P. Czapski, and M. Eiselt. On the influence of volume currents and extended sources on neuromagnetic fields: A simulation study. *Annals of Biomedical Engineering*, 23:728–739, 1995.

[Haueisen *et al.*, 2000] J. Haueisen, C. Ramon, H. Brauer, and H. Nowak. The influence of local conductivity changes on MEG and EEG. *Biomedizinische Technik*, 45(7-8):211–214, 2000.

[Haueisen *et al.*, 2002] J. Haueisen, D.S. Tuch, C. Ramon, P.H. Schimpf, V.J. Wedeen, J.S. George, and J.W. Belliveau. The influence of brain tissue anisotropy on human EEG and MEG. *NeuroImage*, 15:159–166, 2002.

[Haueisen, 1996] J. Haueisen. *Methods of Numerical Field Calculation for Neuromagnetic Source Localization*. PhD thesis, Technical Univ.Ilmenau, 1996.

[Huiskamp *et al.*, 1999] G. Huiskamp, M. Vroeijenstijn, R. van Dijk, G. Wieneke, and A.C. van Huffelen. The need for correct realistic geometry in the inverse EEG problem. *IEEE Trans. Biomed. Eng.*, 46(11):1281–1287, 1999.

[Johnson *et al.*, 2000] C.R. Johnson, M. Mohr, U. Rüde, A. Samsonov, and K. Zyp. Multilevel methods for inverse bioelectric field problems. In R. Bank, T. Barth, and T. Chan, editors, *Yosemite Educational Symposium*, http://raphael.mit.edu/yosemite/, Oct.29–Nov.1, 2000.

[Jung and Langer, 1991] M. Jung and U. Langer. Applications of multilevel methods to practical problems. *Surv.Math.Ind.*, 1:217–257, 1991.

[Karypis and Kumar, 1998] G. Karypis and V. Kumar. METIS – User's Guide. University of Minnesota, http://www-users.cs.umn.edu/ ∼karypis, 1998.

[Kickinger, 1998] F. Kickinger. Algebraic multigrid for discrete elliptic second-order problems. In W. Hackbusch, editor, *Multigrid Meth. V. Proc. of the 5th Europ. Multigrid conf.*, pages 157–172. Springer Lect. Notes Comput. Sci. Eng. 3, 1998.

[Knösche, 1997] T.R. Knösche. *Solutions of the neuroelectromagnetic inverse problem*. PhD thesis, Univ. of Twente, The Netherlands, 1997.

[Koch, 2000] M. Koch. *Measurement of the Self-Diffusion Tensor of Water in the Human Brain*. PhD thesis, Univ. of Leipzig, Germany, 2000.

[Krechel and Stüben, 2001] A. Krechel and K. Stüben. Parallel algebraic multigrid based on subdomain blocking. *Parallel Comp.*, 27(8):1009 – 1031, 2001.

[Latour *et al.*, 1994] L.L. Latour, K. Svoboda, P.P. Mitra, and C.H. Sotak. Time-dependent diffusion of water in a biological model system. *Proc.Natl.Acad.Sci.USA*, 91:1229–1233, 1994.

[Maes *et al.*, 1997] F. Maes, D. Vandermeulen, G. Marchal, and P. Suetens. Multimodality image registration by maximization of mutual information. *IEEE Trans. Med. Imag.*, 16(2):187–198, 1997.

[Maess *et al.*, 2001] B. Maess, S. Koelsch, T.C. Gunter, and A.D. Friederici. Musical syntax is processed in broca's area: an MEG study. *Nature Neuroscience*, 4(5):540–545, 2001.

[Marin *et al.*, 1998] G. Marin, C. Guerin, S. Baillet, L. Garnero, and Meunier G. Influence of skull anisotropy for the forward and inverse problem in EEG: simulation studies using the FEM on realistic head models. *Human Brain Mapping*, 6:250–269, 1998.

[Marin, 1997] G. Marin. *Utilisation de la méthode des éléments finis pour le calcul des champs électromagnétiques à l'aide d'un modèle réaliste de tête en MEG et EEG*. PhD thesis, Université de Paris-Sud, U.F.R. Scientifique d'Orsay, France, 1997.

[Meijs *et al.*, 1989] J.W.H Meijs, O.W. Weier, M.J. Peters, and A. van Oosterom. On the numerical accuracy of the boundary element method. *IEEE Trans. Biomed. Eng.*, 36:1038–1049, 1989.

[Nicholson, 1965] P.W. Nicholson. Specific impedance of cerebral white matter. *Exp.Neurol.*, 13:386–401, 1965.

[Nolting, 1992] W. Nolting. *Grundkurs: Theoretische Physik, Elektrodynamik*. Zimmermann-Neufang, Ulmen, 1992.

[Norris and Börnert, 1993] D.G. Norris and P. Börnert. Coherence and interference in ultra-fast rare experiments. *J. Magn. Reson. A*, 105:123–127, 1993.

[Öztekin *et al.*, 1998] B.U. Öztekin, G. Karypis, and V. Kumar. PMVIS – User's Guide. University of Minnesota, http://www-users.cs.umn.edu/ ∼oztekin/ pmvis/, 1998.

[Pastelak-Price, 1983] C. Pastelak-Price. The international 10-20-system of electrode placement: Its rationale and a practical guide to measuring procedures and electrode placement. *EEG-Labor*, 5:49–72, 1983.

[Payne and Toga, 1990] B.A. Payne and A.W. Toga. Surface mapping brain function on 3D models. *IEEE Computer Graphics & Applications*, 10(5):33–41, 1990.

[Platzer, 1994] W. Platzer, editor. *Pernkopf Anatomie*. Urban & Schwarzenberg, München, 1994.

[Plonsey and Heppner, 1967] R. Plonsey and D. Heppner. Considerations on quasi-stationarity in electro-physiological systems. *Bull.math.Biophys.*, 29:657–664, 1967.

[Pohlmeier, 1996] R. Pohlmeier. Lokalisation elektrischer Gehirnaktivität durch inverse Analyse des Magnetoenzephalogramms (MEG) mit Finite-Elemente-Modellen des Kopfes. Diplomarbeit in Elektrotechnik, RWTH Aachen, 1996.

[Reitzinger, 1999] S. Reitzinger. PEBBLES – User's Guide. SFB F013 "Numerical and Symbolic Scientific Computing", http://www.sfb013.uni-linz.ac.at., 1999.

[Reitzinger, 2001] S. Reitzinger. *Algebraic Multigrid Methods for Large Scale Finite Element Equations*. Number 36 in Schriften der Johannes-Kepler-Universität Linz, Reihe C - Technik und Naturwissenschaften. Universitätsverlag Rudolf Trauner, 2001.

[Ruge and Stüben, 1986] J. W. Ruge and K. Stüben. Algebraic multigrid (AMG). In S. McCormick, editor, *Multigrid Methods*, volume 5 of *Frontiers in Applied Mathematics*, pages 73–130. SIAM, Philadelphia, 1986.

[Sarvas, 1987] J. Sarvas. Basic mathematical and electromagnetic concepts of the biomagnetic inverse problem. *Phys.Med.Biol.*, 32(1):11–22, 1987.

[Scherg and von Cramon, 1985] M. Scherg and D. von Cramon. Two bilateral sources of the late AEP as identified by a spatio-temporal dipole model. *Electroenc. Clin. Neurophysiol.*, 62:32–44, 1985.

[Schimpf *et al.*, 2002] P.H. Schimpf, C.R. Ramon, and J. Haueisen. Dipole models for the EEG and MEG. *IEEE Trans. Biomed. Eng.*, 49(5):409–418, 2002.

[Schmitt and Louis, 2002] U. Schmitt and A.K. Louis. Efficient algorithms for the regularization of dynamic inverse problems-part I: Theory. *Inverse Problems*, 2002. in press.

[Schmitt *et al.*, 2002] U. Schmitt, A.K. Louis, C. Wolters, and M. Vauhkonen. Efficient algorithms for the regularization of dynamic inverse problems-part II: Applications. *Inverse Problems*, 2002. in press.

[Sen *et al.*, 1981] P.N. Sen, C. Scala, and M.H. Cohen. A self-similar model for sedimentary rocks with application to the dielectric constant of fused glass beads. *Geophysics*, 46(5):781–795, 1981.

[SimBio, 2000] SimBio. A generic environment for bio-numerical simulation. IST-program of the European Commission, Project No.10378, http://www.simbio.de, 2000.

[Smythe, 1989] W.R. Smythe. *Static and dynamic electricity*. Hemisphere Publishing, New York, 1989.

[Sutherling *et al.*, 1988] W.W. Sutherling, P.H. Crandall, T.M. Darcey, D.P. Becker, M.F. Levesque, and D.S. Barth. The magnetic and electrical fields agree with intracranial localizations of somatosensory cortex. *Neurology*, 38:1705–1714, 1988.

[Tuch *et al.*, 1998] D.S. Tuch, V.J. Wedeen, A.M. Dale, and J.W. Belliveau. Electrical conductivity tensor map of the human brain using NMR diffusion imaging: An effective medium approach. *ISMRM, 6th Scientific Meeting, Sydney*, 1998.

[Tuch *et al.*, 1999] D.S. Tuch, V.J. Wedeen, A.M. Dale, J.S. George, and J.W. Belliveau. Conductivity mapping of biological tissue using diffusion MRI. *Ann. NYAS*, 888:314–316, 1999.

[van den Broek *et al.*, 1997] S.P. van den Broek, M. Donderwinkel, and M.J. Peters. The influence of inhomogenities in a realistically shaped volume conductor on EEG and MEG. In H. Witte, U. Zwiener, B. Schack, and A. Doering, editors, *Quantitative and Topological EEG and MEG Analysis*, pages 456–458. Druckhaus Mayer Verlag GmbH Jena · Erlangen, 1997.

[van den Broek, 1997] S.P. van den Broek. *Volume Conduction Effects in EEG and MEG*. PhD thesis, Proefschrift Universiteit Twente Enschede, The Netherlands, 1997.

[Waberski *et al.*, 1998] T.D. Waberski, H. Buchner, K. Lehnertz, A. Hufnagel, M. Fuchs, R. Beckmann, and A. Rienäcker. The properties of source localization of epileptiform activity using advanced headmodelling and source reconstruction. *Brain Top.*, 10(4):283–290, 1998.

[Wagner, 1998] M. Wagner. *Rekonstruktion neuronaler Ströme aus bioelektrischen und biomagnetischen Messungen auf der aus MR-Bildern segmentierten Hirnrinde*. PhD thesis, Shaker-Verlag Aachen, 1998.

[Wagner, 2000] C. Wagner. On the algebraic construction of multilevel transfer operators. *Computing*, 65:73–95, 2000.

[Wang *et al.*, 2001] Y. Wang, D.R. Haynor, and Y. Kim. An investigation of the importance of myocardial anisotropy in finite-element modeling of the heart: Methodology and application to the estimation of defibrillation efficacy. *IEEE Trans. Biomed. Eng.*, 48(12), 2001.

[Wolters *et al.*, 1999a] C.H. Wolters, R.F. Beckmann, A. Rienäcker, and H. Buchner. Comparing regularized and non-regularized nonlinear dipole fit methods: A study in a simulated sulcus structure. *Brain Top.*, 12(1):3–18, 1999.

[Wolters *et al.*, 1999b] C.H. Wolters, U. Hartmann, M. Koch, F. Kruggel, S. Burkhardt, A. Basermann, D.S. Tuch, and J. Haueisen. New methods for improved and accelerated FE volume conductor modeling in EEG/MEG-source reconstruction. In J. Middleton, M. Jones, N. Shrive, and G. Pande, editors, *4th Symp. on Computer Methods in Biomech. and Biomed.Eng.*, pages 489–494, Lisboa, Okt.31–Nov.3 1999. Gordon & Breach.

[Wolters *et al.*, 2000] C. Wolters, S. Reitzinger, A. Basermann, S. Burkhardt, U. Hartmann, F. Kruggel, and A. Anwander. Improved tissue modeling and fast solver methods for high resolution FE-modeling in EEG/MEG-source localization. In J. Nenonen, R.J. Ilmoniemi, and T. Katila, editors, *Proc. of the 12th Int.Conf.of Biomagnetism*, pages 655–658, http://biomag2000.hut.fi/papers_all.html, Aug.13–17, 2000.

[Wolters *et al.*, 2002] C.H. Wolters, M. Kuhn, A. Anwander, and S. Reitzinger. A parallel algebraic multigrid solver for finite element method based source localization in the human brain. *Comp.Vis.Sci.*, 2002. in press.

[Wolters, 2002] C. Wolters. *Influence of tissue conductivity inhomogeneity and anisotropy to EEG/MEG based source localization in the human brain*. PhD thesis, University of Leipzig, 2002. in preparation.

[Zanow and Peters, 1995] F. Zanow and M.J. Peters. Individually shaped volume conductor models of the head in EEG source localisation. *Med. & Biol. Eng. & Comput.*, 7:151–161, 1995.

[Zhou and van Oosterom, 1992] H. Zhou and A. van Oosterom. Computation of the potential distribution in a four-layer anisotropic concentric spherical volume conductor. *IEEE Trans. Biomed. Eng.*, 39(2):154–158, 1992.